RSC Advances

PAPER

View Article Online
View Journal | View Issue

Cite this: *RSC Adv.*, 2026, **16**, 28452

Synergetic mono- and bimetallic tungstate–biochar composites for efficient adsorptive removal of aniline blue from simulated wastewater: reusability, multivariate analysis, and greenness assessment

Kizhan S. Rostam and Khanda F. M. Amin *

The removal of synthetic dyes from industrial wastewater remains a significant environmental challenge due to their high chemical stability and resistance to biodegradation. This study presents a comparative evaluation of three tungstate-modified loquat biochar composites $ZnWO_4$/loquat biochar (ZW/LB), $MnWO_4$/loquat biochar (MW/LB), and bimetallic Zn–Mn–WO_4/loquat biochar (ZMW/LB) for the adsorption of aniline blue under both deionized water and simulated wastewater conditions, highlighting the influence of ionic competition on mono- and bimetallic systems. Comprehensive characterization using XRD, FTIR, FESEM, BET, EDX, and ICP-OES confirmed the successful formation of crystalline tungstate phases and mesoporous structures with enhanced surface properties. Batch adsorption experiments were conducted to investigate the effects of pH, contact time, initial dye concentration, temperature, and adsorbent dosage. The adsorption process was well described by pseudo-second-order kinetics and predominantly followed Langmuir-type behavior; however, it is more accurately attributed to a combination of electrostatic interactions, surface complexation, and diffusion processes. Among the synthesized materials, ZMW/LB achieved the highest removal efficiency in deionized water (89.16 ± 0.73%), while ZW/LB exhibited superior performance in simulated wastewater (89.33 ± 1.93%), indicating enhanced resistance to ionic interference. MW/LB showed comparatively lower adsorption efficiency but more stable performance under varying conditions. Reusability studies confirmed high structural stability, with removal efficiencies remaining above 95% after five cycles. Multivariate analysis revealed that textural properties account for 76.24% of adsorption performance, highlighting the dominant role of pore structure and surface area. Mass balance analysis demonstrated that Zn-containing composites require lower adsorbent dosages, confirming improved material efficiency. Furthermore, combined environmental evaluation using Eco-Scale, AGREE, GAPI, and simplified life cycle analysis indicated that ZW/LB exhibits the lowest environmental footprint when normalized to adsorption performance. Overall, the developed tungstate–biochar composites, particularly ZW/LB, show strong potential as efficient, reusable, and environmentally sustainable adsorbents for dye removal in complex wastewater systems.

Received 27th March 2026
Accepted 18th May 2026

DOI: 10.1039/d6ra02562e

rsc.li/rsc-advances

1 Introduction

Water quality and ecosystem sustainability are seriously at risk due to a substantial increase in the discharge of chemical pollutants into aquatic environments as a result of industrial development.[1] Among these pollutants, synthetic dyes released from textile, paper, and related industries are of particular concern due to the complicated aromatic structures and remarkable chemical stability.[2] These substances can persist in water systems for extended periods and are often resistant to natural degradation processes. Even at relatively low concentrations, dye contaminants may reduce light penetration in water reservoirs, disturb photosynthetic activity of aquatic plants and algae, and, in some cases, exhibit toxic or mutagenic effects on living organisms.[3,4]

Aniline blue (AB) is a common anionic dye used in biological staining, paper manufacturing, and textile dyeing. This dye is particularly difficult to remove from wastewater due to its high solubility and chemical stability, which allow it to persist in aquatic environments for long periods.[5,6] As a consequence, the development of efficient and sustainable treatment techniques

---

Department of Chemistry, College of Science, University of Sulaimani, Qlyasan Street, Kurdistan Regional Government, Sulaymaniyah, 46001, Iraq. E-mail: khanda.mohammed@univsul.edu.iq

for the elimination of dye pollution has become a crucial field of research.[7]

Recently, several treatment strategies, including chemical oxidation, membrane filtration, photocatalytic degradation, and biological treatment techniques, have been investigated for the dye removal.[8–10] Although these techniques can achieve acceptable removal efficiency under certain circumstances, they have drawbacks, including high running costs, energy consumption, residual pollutants, and complex operational requirements.[11] Due to its high removal efficiency, ease of use, affordability, and flexibility in adsorbent design, adsorption technology has emerged as one of the most promising and useful methods for treating wastewater.[12] Moreover, adsorption processes generally produce minimal secondary pollutants and allow the possibility of adsorbent regeneration and reuse, which further enhances their sustainability economically and environmentally.[13]

However, activated carbon has traditionally been considered the most effective adsorbent for removing dye; its large-scale application is frequently limited by high production costs, energy-intensive activation processes, and gradual loss of adsorption capacity after repeated regeneration cycles. These restriction have more widely utilized in the development of low-cost and sustainable adsorbent materials derived from biomass resources.[14] Biochar produced from agricultural waste has received considerable concern based on the structure porous, abundant surface functional groups, chemical stability, and environmentally friendly nature.[15]

Despite its effectiveness, conventional activated carbon is limited by high production cost and energy-intensive activation processes. This has driven increasing interest in low-cost, biomass-derived adsorbents such as biochar.[14] Loquat (*Eriobotrya japonica*) seeds constitute an abundant and underused agricultural biomass with high carbon content and favorable physicochemical properties for the formation of biochar. Biochar materials possess porous structures, abundant surface functional groups, and good chemical stability, making them attractive candidates for pollutant removal.[15] However, pristine biochar often exhibits limited adsorption selectivity and relatively moderate adsorption capacity, which restricts its practical application in wastewater treatment systems. Extensive research has focused on improving the adsorption performance of biochar through surface modification, activation, or the incorporation of functional nanomaterials.[16,17] Among modification strategies, an effective technique to improve adsorption capability is the incorporation of metal-based nanostructures into biochar matrices.[18]

Metal tungstates (MWO_4) such as $ZnWO_4$ and $MnWO_4$ have gained increasing interest due to their excellent chemical stability, structural robustness, and rich metal–oxygen surface chemistry.[19–22] These materials provide abundant active sites that can interact with organic contaminants through surface complexation, electrostatic attraction, and hydrogen bonding. Furthermore, their semiconductor properties have been widely studied in photocatalysis and environmental remediation applications.[23,24]

Monometallic tungstate systems may exhibit limitations despite these benefits, such as restricted access to the active site and moderate adsorption capacity.[25] Bimetallic tungstate systems, particularly Zn–Mn–WO_4 materials, have recently attracted interest to overcome these drawbacks.[26] The incorporation of two divalent metal ions into the tungstate lattice can introduce structural defects, increase surface heterogeneity, and generate additional adsorption sites, thereby improving adsorption performance through synergistic interactions between the metal centers. The resulting hybrid composites may exhibit enhanced surface area, improved dispersion of active components, and superior adsorption behavior when such materials are supported on porous carbonaceous matrices such as biochar.[27–29] Dutta and co-workers reported the sorption behavior of nanocrystalline $MnWO_4$/$MnMoO_4$ synthesized through a sonochemical approach.[30]

Nevertheless, studies investigating tungstate–biochar hybrid composites for dye adsorption remain limited, particularly for bimetallic Zn–Mn–WO_4 systems. In addition, the adsorption performance of such materials under realistic conditions, such as simulated wastewater containing competing ions, has rarely been explored. The incorporation of Zn and Mn within the tungstate structure supported on porous biochar is expected to create a defect-rich and heterogeneous surface in order to improve both adsorption capacity and interaction with anionic dye molecules such as aniline blue.

In this context, the present study develops and evaluates three loquat biochar-based composites: $ZnWO_4$/loquat biochar (ZW/LB), $MnWO_4$/loquat biochar (MW/LB), and a bimetallic Zn–Mn–WO_4/loquat biochar (ZMW/LB). The adsorption performance of these materials toward aniline blue was systematically investigated under both deionized water and simulated wastewater conditions to assess the effect of ionic competition and solution complexity.

PH, contact time, initial dye concentration, adsorbent dose, and temperature are the key operational parameters; their impacts were methodically evaluated to identify the optimal adsorption conditions. Comprehensive characterization (XRD, FTIR, FESEM, BET, EDX, and ICP-OES) was conducted to elucidate structural and surface properties. Adsorption behavior was analyzed using kinetic, isotherm, and thermodynamic models, complemented by multivariate statistical analysis, PCA[31] and HCA[32] to explore correlations between physicochemical properties and adsorption performance. Importantly, the study integrates mass balance evaluation, regeneration analysis, and preliminary life cycle considerations to provide a more realistic assessment of scalability and environmental sustainability was assessed using green chemistry metrics Eco-Scale,[33] AGREE,[34] and GAPI.[35] This integrated approach provides deeper insight into the structure–performance relationship of tungstate–biochar composites and highlights their potential as efficient and sustainable adsorbents for dye-contaminated wastewater treatment.

The novelty of this work lies not only in the development of a bimetallic tungstate–biochar composite but also in the comprehensive and application-oriented evaluation framework, which bridges the gap between laboratory-scale performance and real-world applicability. The findings provide critical insight into the design of efficient, reusable, and environmentally sustainable adsorbents for wastewater treatment.

2 Materials and methods

2.1 Materials

Analytical-grade chemicals and solvents were obtained from Merck and Sigma-Aldrich, which were used without any additional purification. Zinc nitrate hexahydrate ($Zn(NO_3)_2 \cdot 6H_2O$), sodium tungstate dihydrate ($Na_2WO_4 \cdot 2H_2O$), magnesium sulfate hexahydrate ($MgSO_4 \cdot 6H_2O$), calcium chloride dihydrate ($CaCl_2 \cdot 2H_2O$), sodium chloride (NaCl), ethanol (C_2H_2OH), ammonia solution (NH_4OH), nitric acid (HNO_3), hydrochloric acid (HCl), sodium hydroxide (NaOH). Deionized (DIW) water was utilized throughout the investigation.

2.2 Synthesis of loquat seed biochar (LB)

Loquat seeds were washed thoroughly using DI water before being dried at 80 °C for more than 12 hours. In a tube furnace with nitrogen flow (100 mL min^{-1}) and an average temperature of 10 °C min^{-1} up to 500 °C, the dried seeds were pyrolyzed for two hours. After cooling under nitrogen, the obtained biochar was ground and sieved (200 μm), yielding approximately 30–40%. For activation, the biochar was dispersed in DI water, stirred for 15 min, filtered, and then dried overnight at 60–80 °C. Chemical activation was performed by treating the dried biochar with a small amount of nitric acid, followed by drying to eliminate any remaining moisture.[16]

2.3 Synthesis of mono- and bimetallic composites

2.3.1 Synthesis of $MnWO_4$/biochar nanocomposite (MW/LB). $MnWO_4$/biochar nanocomposite was synthesized *via* a hydrothermal *in situ* growth approach. $MnCl_2 \cdot 4H_2O$ (0.989 g, 5.0 mmol) and $Na_2WO_4 \cdot 2H_2O$ (1.680 g, 5.0 mmol) were separately dissolved in 35 mL of deionized water (DIW) to obtain two clear precursor solutions under magnetic stirring. The solutions were subsequently combined while being continuously stirred to facilitate the formation of $MnWO_4$, and 0.1 M NaOH was used to adjust the pH of the resulting mixture to 8.0. Disperse 0.5 g biochar into 30 mL DI water in a beaker; sonicate 20–30 min to wet and deagglomerate. The prepared precursor solution was then added dropwise to a well-dispersed suspension of activated biochar under vigorous stirring to promote *in situ* nucleation and homogeneous deposition of $MnWO_4$ nanoparticles onto the biochar surface. To guarantee consistent interaction between the metal precursors and the biochar matrix, the suspension was further stirred for 15 min. To assist the hydrothermal process to proceed, the prepared mixture was placed in a 150 mL stainless-steel autoclave walled with Teflon and kept at 160 °C for 16 h. After completion, the autoclave was left to cool to room temperature, and filtration was used to separate the solid formed. The recovered material was washed several times with DIW until the washings were free of chloride ions, which was verified using a silver nitrate ($AgNO_3$) test. To further remove possible residual species, the product was additionally rinsed with ethanol. The purified solid was then dried overnight at 70–80 °C. Subsequently, a thermal treatment was carried out at 330 °C for 2 h under restricted oxygen conditions to enhance the crystallinity of the material and promote stronger interaction between $MnWO_4$ particles and the biochar support. The obtained composite was designated as MW/LB.

2.3.2 Synthesis of $ZnWO_4$/biochar nanocomposite (ZW/LB). The $ZnWO_4$/biochar nanocomposite was prepared *via* a hydrothermal *in situ* growth method. $Zn(NO_3)_2 \cdot 6H_2O$ (1.487 g, 5.00 mmol) and $Na_2WO_4 \cdot 2H_2O$ (1.649 g, 5.00 mmol) were separately dissolved in 50 mL of DIW, under continuous magnetic stirring to obtain clear precursor solutions. The tungstate solution was then slowly added to the zinc precursor solution under vigorous stirring, to facilitate the formation of $ZnWO_4$. The pH of the mixture was adjusted to 8 using 0.1 M NH_4OH, and the resulting suspension was stirred at room temperature to ensure complete precursor interaction. Disperse 0.5 g biochar into 30 mL DI water in a beaker; sonicate 20–30 min to wet and deagglomerate. The prepared precursor solution was then added dropwise to a well-dispersed suspension of activated biochar under vigorous stirring to promote *in situ* nucleation and homogeneous deposition of $ZnWO_4$ nanoparticles onto the biochar surface. To proceed with the hydrothermal process, the prepared mixture was placed in a 150 mL stainless-steel autoclave walled with Teflon and kept at 160 °C for 16 h. After completion, the autoclave was left to cool to room temperature, and filtration was used to separate the solid formed. It was then extensively cleaned with deionized water to get rid of any remaining ions before being rinsed with ethanol. To improve crystallinity and fortify the bond between $ZnWO_4$ nanoparticles and the biochar, the material was further dried at 70–80 °C for a whole night before being calcined at 330 °C for two hours under low oxygen circumstances. ZW/LB was the composite that was produced.

2.3.3 Synthesis of bimetallic Zn–Mn–WO_4/biochar (ZMW/LB). The bimetallic Zn–Mn–WO_4/biochar nanocomposite was synthesized *via* the same hydrothermal *in situ* growth procedure. $MnCl_2 \cdot 4H_2O$ (0.890 g, 4.5 mmol) and $Zn(NO_3)_2 \cdot 6H_2O$ (0.149 g, 0.5 mmol) were separately dissolved in 20 mL DI water, while $Na_2WO_4 \cdot 2H_2O$ (1.683 g, 5.0 mmol) was dissolved in 30 mL DI water. This composition corresponds to a $Zn_{0.1}Mn_{0.9}WO_4$ stoichiometry. The metal precursor solutions were combined and stirred vigorously, after which the tungstate solution was slowly introduced while maintaining a pH of 8 using 0.1 M NaOH. Disperse 0.5 g biochar into 30 mL DI water in a beaker; sonicate for 20–30 min. The prepared precursor solution was then added dropwise to a well-dispersed suspension of activated biochar and stirred for 20 min, promoting *in situ* nucleation and uniform growth of Zn–Mn tungstate nanoparticles on the biochar surface. The resulting suspension was transferred into a 150 mL Teflon-lined autoclave and heated at 170 °C for 24 h. After natural cooling, the solid product was filtered and washed repeatedly with hot DIW to remove residual ions, followed by ethanol washing. The composite was dried overnight at 80 °C and finally calcined at 330 °C for 2 h under limited oxygen conditions to obtain the ZMW/LB nanocomposite.

Stoichiometric composition of the synthesized composites were presented in Fig S1.

2.4 Materials characterization

The structural, chemical, and morphological properties of the composites were comprehensively analyzed. X-ray diffraction (XRD, Shimadzu 6000) was used to identify crystalline phases, while Fourier-transform infrared spectroscopy (FTIR, PerkinElmer) revealed the surface functional groups. Field-emission scanning electron microscopy (FESEM, Zeiss Auriga) provided insights into the microstructure and surface morphology, and the Brunauer–Emmett–Teller (BET) method (NOVA 4200e, Quantachrome) was employed to assess the specific surface area and pore characteristics. The metal content and elemental composition were further quantified by inductively coupled plasma (ICP-OES) analysis, ensuring precise determination of the bimetallic ratios in the composites.

2.5 Batch adsorption experiments

In conical flasks, 50 mL of aniline blue solution (100 mg L^{-1}) and 0.015 g of adsorbent were combined for batch adsorption analysis. To achieve equilibrium, the suspensions were agitated at 150 rpm for 120 minutes at room temperature. Following adsorption, the mixtures were centrifuged, the residual dye concentration (C_e) at $\lambda_{max} = 597$ nm was measured using UV-vis spectrophotometry. The following formulas were used to calculate the equilibrium adsorption capacity (q_e) and removal effectiveness (R%), as shown in eqn (1) and (2):[29,36]

$$\text{Removal }\%(R\%) = \frac{C_0 - C_e}{C_0} \times 100 \quad (1)$$

$$q_e(\text{mg g}^{-1}) = \frac{(C_0 - C_e)v}{m} \quad (2)$$

where C_0 and C_e (mg L^{-1}) are the initial and equilibrium concentrations, m (g) is the adsorbent mass, and V (L) is the solution volume.

Adsorption was methodically examined in accordance with temperature (25–45 °C), adsorbent dose (10–200 mg), initial dye concentration (5–300 mg L^{-1}), and contact time (0–180 min). To elucidate the process kinetics and isotherms models were analyzed.

The point of zero charge (pH_{pzc}) of the adsorbents was determined by adding 50 mg of adsorbent to 50 mL of 0.01 M NaCl solution, with the starting pH adjusted between 2 and 11. The suspensions were shaken for 24 hours to estimate pH_{pzc}, and the final pH values were noted.

The statistical analysis was performed to confirm the accuracy of the measurement results and good fit of the experimental adsorption data with the proposed models. The results were examined using (SSE), the sum of the squared error and (X^2), the Chi-square test.[37] Both metrics were determined through the use of eqn (3) and (4), respectively. The equations of all error functions used are expressed as follows:

$$X^2 = \sum_{i=1}^{n} \left(\frac{q_e - q_c}{q_e}\right)^2 \quad (3)$$

$$\text{SSE} = \sum_{i=1}^{n} (q_e - q_c)^2 \quad (4)$$

where, q_c and q_e (mg g^{-1}) are the theoretical and the experimental adsorption capacity at equilibrium.

2.6 Adsorption in simulated wastewater (SWW)

Simulated wastewater was prepared by dissolving aniline blue (100 mg L^{-1}) in DI water containing NaCl (1000 mg L^{-1}), $CaCl_2 \cdot 2H_2O$ (100 mg L^{-1}), and $MgSO_4 \cdot 6H_2O$ (100 mg L^{-1}). Adsorption experiments were conducted under identical conditions as in DI water. The data are shown as mean ± standard deviation, and each experiment was conducted in triplicate.

2.7 Adsorption–desorption and reusability procedure

Through consecutive adsorption–desorption cycles, the adsorbent's reusability was evaluated in simulated wastewater to mimic practical operating conditions. The spent adsorbent after each adsorption experiment was recovered by centrifugation, treated with 0.1 M NaOH and subjected to a 2 h agitation to desorb the dye. The desorption efficiency (%) and reusability (%) were calculated by using eqn (5) and (6):

$$\%\text{ desorption} = \frac{q_{des}}{q_{ads}} \times 100 \quad (5)$$

$$\%\text{ reusability} = \frac{q_n}{q_1} \times 100 \quad (6)$$

The amounts of dye desorbed and adsorbed are represented by q_{des} and q_{ads}, respectively, while the reusability% in the first cycle was % 100 as a ref. 38.

The regenerated adsorbent was dried after being washed with DIW to neutral pH, and reused in a subsequent batch under identical conditions. This cycle was repeated up to five times, and the adsorption efficiency was monitored after each run to assess the material's performance retention.

3 Result and discussion

3.1 Characterization of materials

3.1.1 XRD-phase formation and crystallinity. The XRD patterns of LB, MW/LB, ZW/LB, and ZMW/LB are presented in Fig. 1 and S1. Pristine LB exhibits a broad diffraction band centered at $\sim 2\theta = 24.1°$ corresponding to the (002) plane and a weak peak at ~44.6° assigned to the (100) plane,[39] confirming it's amorphous and turbostratic carbon structure with low crystallinity.

For the ZW/LB composite (reference code 96-210-1677), as shown in Fig. 2, several sharp diffraction peaks were observed at 2θ values of 18.5°, 23.1°, 28.8–29.0°, 30.6°, 34.6°, and 36.4°, which are indexed to the (010), (100), (011), (110), (111), and (021) planes of monoclinic $ZnWO_4$. The disappearance of the

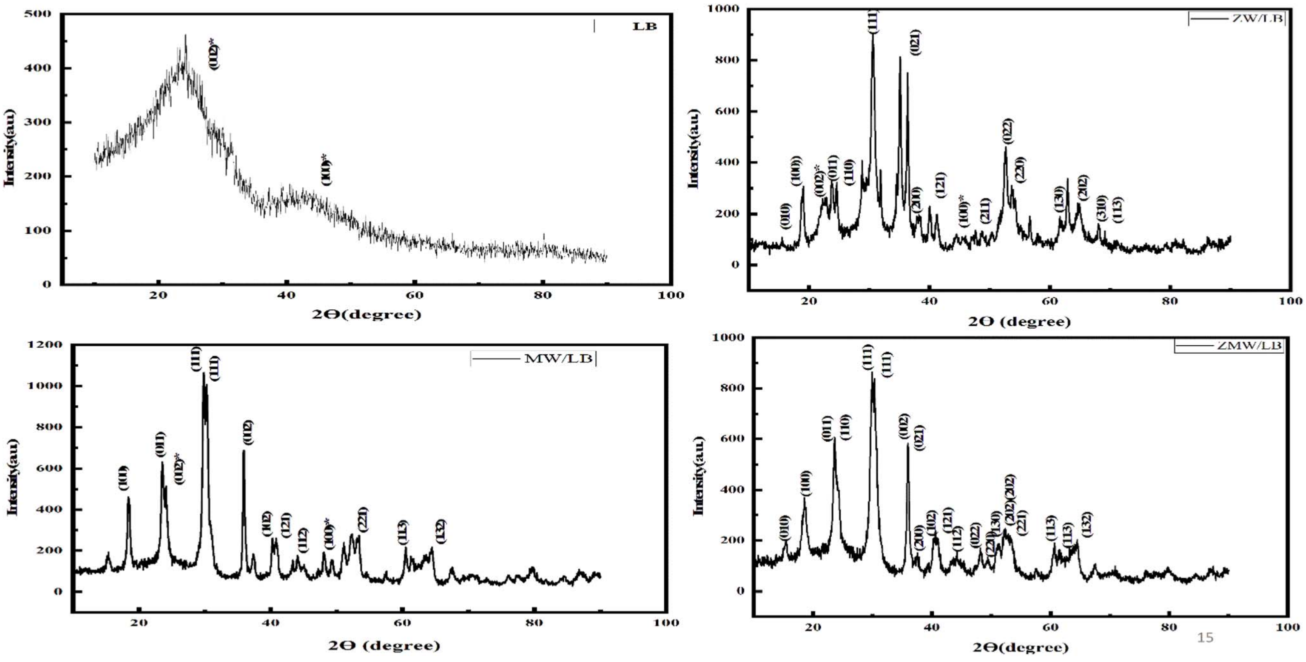

Fig. 1 Random powder XRD pattern of LB, MW/LB, ZW/LB, and ZMW/LB.

broad carbon hump indicates that the crystalline $ZnWO_4$ phase dominates the diffraction pattern.[40,41] No secondary phases such as ZnO or WO_3 were detected, confirming phase purity.

Similarly, the MW/LB composite (reference code 96-591-0348), as shown in Fig. 2, exhibits characteristic peaks at $2\theta \approx 29.85°$ (111) along with reflections at 18.4°, 23.55°, 30.25°, 35.95°, 40.25°, 40.85°, 44.1°, 53.4°, 60.5°, and 64.5° can be

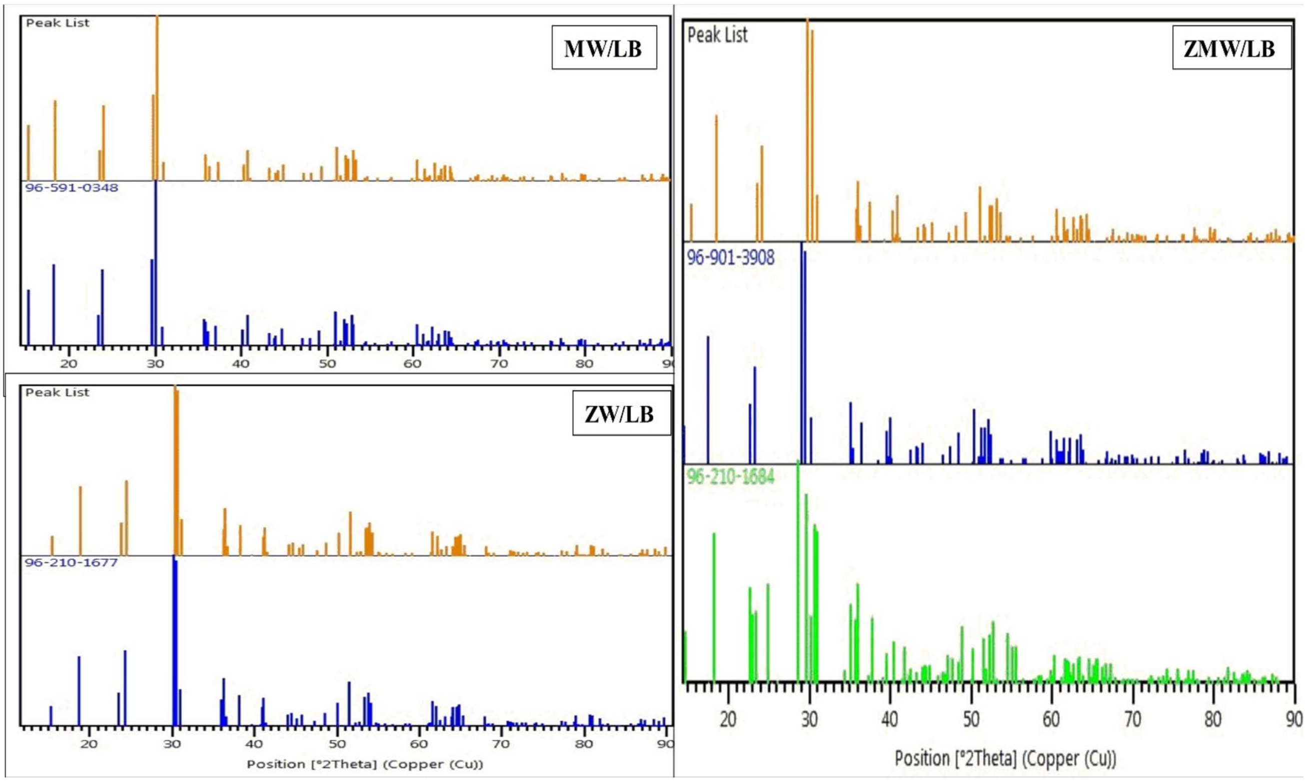

Fig. 2 Random powder XRD pattern of LB, MW/LB, ZW/LB, and ZMW/LB compared to the standard reference.

indexed to the (100), (011), (111), (002), (102), (121), (112), (221), (113), and (132) crystal planes, respectively, corresponding to monoclinic $MnWO_4$. Minor broad features at higher angles are attributed to the amorphous biochar matrix.[42]

In the bimetallic ZMW/LB composite, the diffraction peaks closely match both $ZnWO_4$ and $MnWO_4$ phases, with slight peak shifts and overlapping reflections. Characteristic reflections corresponding to both $ZnWO_4$ and $MnWO_4$ phases were observed, with slight peak shifts and overlapping features, confirming the formation of a $Zn_xMn_{1-x}WO_4$ solid solution. The absence of peak splitting further supports the successful incorporation of Zn^{2+} into the $MnWO_4$ lattice. The formation of the solid solution is consistent with the Hume-Rothery rules, as the ionic radii of Zn^{2+} (~74 pm) and Mn^{2+} (~80 pm) differ by less than 15%, allowing substitution within the same crystal lattice.[43,44] No impurity peaks were detected, confirming the high purity of the synthesized materials, as shown in Fig. 2. Overall, XRD analysis confirms the successful formation of crystalline mono- and bimetallic tungstate phases uniformly supported on amorphous biochar.

3.1.2 Structural model. Structurally, $ZnWO_4$ and $MnWO_4$ adopt a wolframite-type lattice composed of $[WO_6]$ octahedral linked with $[ZnO_6]$ or $[MnO_6]$ octahedra through shared oxygen atoms. In the bimetallic system, partial substitution of Mn^{2+} by Zn^{2+} results in the formation of a $Zn_xMn_{1-x}WO_4$ solid solution while preserving the WO_6 framework. The structure is stabilized through Zn–O–W and Mn–O–W linkages.[30,45] When supported on biochar, these tungstate phases interact with surface oxygenated functional groups, forming interfacial M–O–C bonds (M = Zn, Mn, W), which enhance anchoring and structural stability.

3.1.3 Functional group analysis by FTIR spectroscopy. The FTIR spectra of LB, MW/LB, ZW/LB, and ZMW/LB are shown in Fig. 3. Pristine LB exhibits a broad O–H stretching band at 3132–3013 cm^{-1}, attributed to hydroxyl groups and adsorbed moisture. Bands at 1693 and 1572 cm^{-1} correspond to C=O and aromatic C=C stretching, confirming the carbonaceous structure. The peak at 1050 cm^{-1} is assigned to C–O stretching, while bands at 872–749 cm^{-1} indicate aromatic C–H bending.[46,47] After metal incorporation, noticeable spectral changes occur. In MW/LB, slight shifts in O–H and C=O bands indicate coordination between Mn^{2+} ions and oxygen-containing functional groups. A new band at ~575 cm^{-1} confirms Mn–O vibration, indicating $MnWO_4$ formation. For ZW/LB, broadened O–H bands and shifts in the 1580–1400 cm^{-1} region suggest Zn^{2+} coordination. The appearance of bands at ~572 and 469 cm^{-1} corresponds to Zn–O vibrations, confirming $ZnWO_4$ formation.[48,49] The bimetallic ZMW/LB spectrum combines features of both systems. Enhanced C–O stretching (~1057 cm^{-1}) and overlapping bands in the 866–421 cm^{-1} region confirm the coexistence of Zn–O, Mn–O, and W–O bonds. Slight band shifts further support the formation of a $Zn_xMn_{1-x}WO_4$ solid solution.[50] Overall, FTIR results confirm successful anchoring of mono- and bimetallic tungstate phases onto the biochar surface through metal–oxygen interactions.

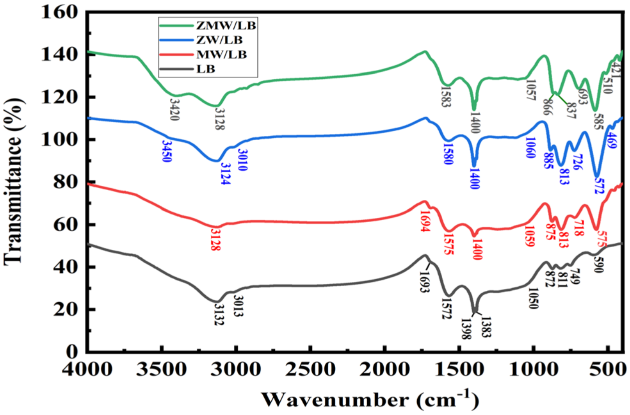

Fig. 3 Fourier transformation infrared (FTIR) for LB, MW/LB, ZW/LB, and ZMW/LB.

3.1.4 FESEM – morphology and dispersion. The surface morphology of the prepared composites was investigated by field emission scanning electron microscopy (FESEM), as illustrated in Fig. 4.

The FESEM images revealed that the biochar support exhibits a rough and porous surface structure, which provides abundant active sites for the deposition of metal tungstate particles. After the hydrothermal synthesis, the metal tungstates were successfully anchored onto the biochar matrix, forming irregularly distributed nanoparticles on the surface.

In the MW/LB composite, $MnWO_4$ particles appeared as small aggregated clusters dispersed over the porous biochar framework. For the ZW/LB material, $ZnWO_4$ particles were observed to be relatively well distributed, partially covering the biochar surface while maintaining the porous structure. In the case of the hybrid ZMW/LB composite, the morphology showed a more compact structure with mixed Mn–Zn tungstate nanoparticles attached to the carbon matrix, indicating the successful formation of the hybrid phase.

The MW/LB composite exhibited a highly porous and irregular structure characteristic of biochar, with the surface decorated by granular and clustered particles.[13] At higher magnifications, these particles appeared as nano- to submicron-sized agglomerates distributed across the surface and embedded within pores. This morphology indicates the successful deposition of $MnWO_4$ onto the biochar, although some degree of particle aggregation was observed, which is typical for metal oxide systems.

Similarly, the ZW/LB composite displayed a rough and porous surface with uniformly distributed fine particles. The $ZnWO_4$ particles appeared as small agglomerates anchored on the biochar surface and within its pores. Compared to $MnWO_4$, the $ZnWO_4$ particles showed relatively improved dispersion, although mild aggregation was still present. The deposition of $ZnWO_4$ increased the surface roughness, indicating the successful functionalization of the biochar.

In contrast, the bimetallic ZMW/LB composite demonstrated a more homogeneous and refined morphology. The surface was densely covered with smaller and more uniformly distributed nanoparticles, with significantly reduced aggregation compared to the monometallic counterparts.[51] The particles were well

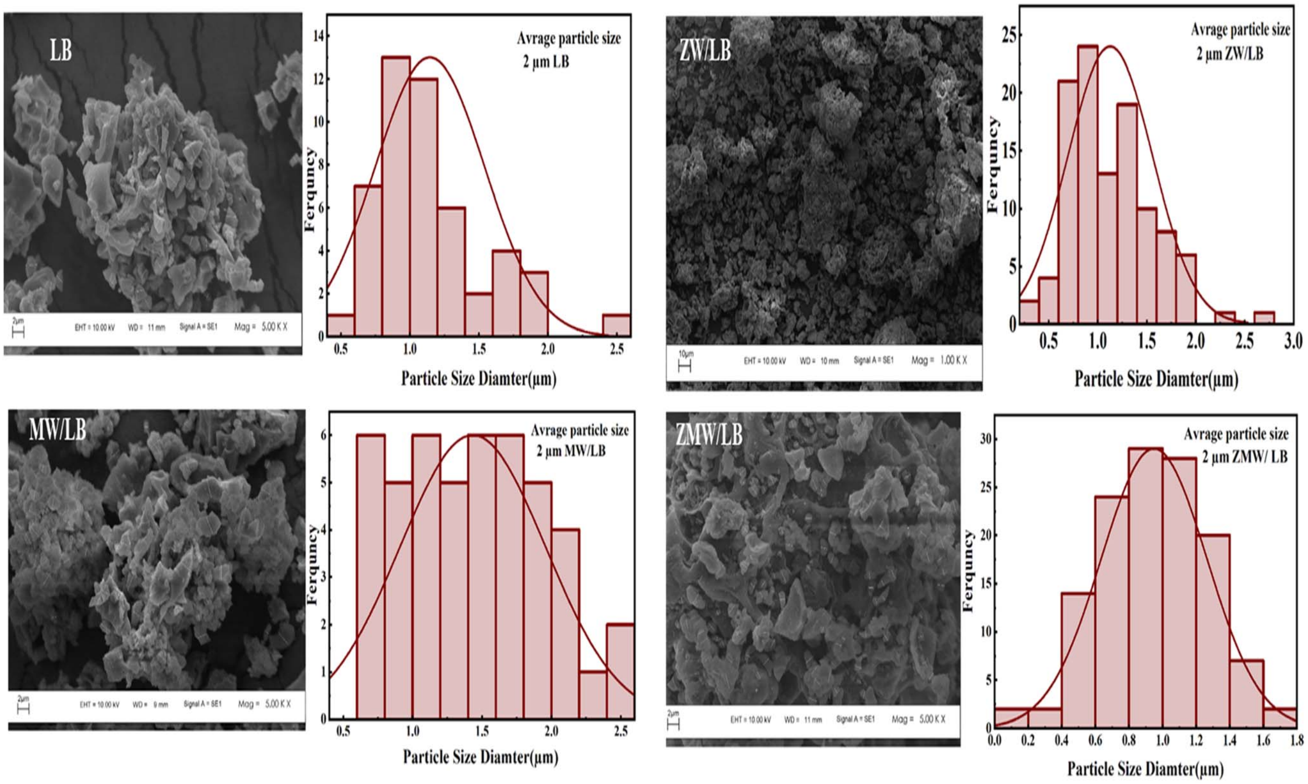

Fig. 4 FESEM and particle size distribution for LB, MW/LB, ZW/LB, and ZMW/LB.

anchored within the pores and surface defects of the biochar, preserving its porous structure. This improved dispersion is attributed to the synergistic effect between Zn and Mn during the nucleation and growth process, which inhibits excessive crystal growth and promotes uniform particle formation.

Overall, FESEM analysis confirms that the incorporation of metal tungstates significantly modifies the surface morphology of biochar. While monometallic composites exhibit noticeable particle aggregation, the bimetallic ZMW/LB displays finer, more uniformly distributed nanoparticles with reduced agglomeration. This improved dispersion enhances surface homogeneity and increases the availability of active adsorption sites, which is expected to contribute to superior adsorption performance.

3.1.5 EDX analysis. The elemental composition of the produced biochar-based composites was examined, and the effective integration of metal tungstate phases was verified, using energy-dispersive X-ray (EDX) analysis.[13,51] Fig. 5 highlights the heterogeneity of biochar and the composite, as well as the EDX spectrum of LB, which consists mainly of carbon and oxygen, along with minerals such as P, S, K, Mg, Cl, and Ca.

For the MW/LB composite, the EDX spectrum revealed the presence of C, O, Mn, and W, as the main elements. The high carbon content confirms the biochar matrix, while the simultaneous detection of Mn and W verifies the successful formation of manganese tungstate. Oxygen was found to be the dominant element, consistent with the oxide nature of $MnWO_4$.

In the case of the ZW/LB composite, the EDX results confirmed the presence of Zn, W, O, and C. The relatively high carbon percentage reflects the dominance of the biochar support, while the detection of Zn and W confirms the formation of zinc tungstate on the biochar surface. As in the Mn-based composite, oxygen was the major element owing to the oxide framework. The tungsten content appeared comparatively lower than zinc, which is commonly observed due to the weaker M-line emission of tungsten and the influence of the carbon-rich matrix. Trace chlorine was also detected, indicating minor residual impurities from precursor salts.

For the bimetallic ZMW/LB composite, the EDX spectrum demonstrated the coexistence of Zn, Mn, W, O, and C, confirming the successful incorporation of both metals within the tungstate structure. Notably, the atomic percentages of (Mn and W) were nearly equivalent, suggesting the formation of a $MnWO_4$-type framework. At the same time, the presence of Zn indicates its effective substitution or incorporation into the lattice, forming a $Zn_xMn_{1-x}WO_4$ solid solution.[45] This balanced elemental distribution provides strong evidence for the successful synthesis of a homogeneous bimetallic system rather than a simple physical mixture of individual oxides.

The effective development of mono- and bimetallic tungstate phases on the surface of the biochar is generally confirmed by the EDX data. The efficiency of the synthesis process is shown by the constant presence of C, O, and metal species as well as the lack of notable contaminants. Minor discrepancies in elemental percentages are attributed to the semi-quantitative

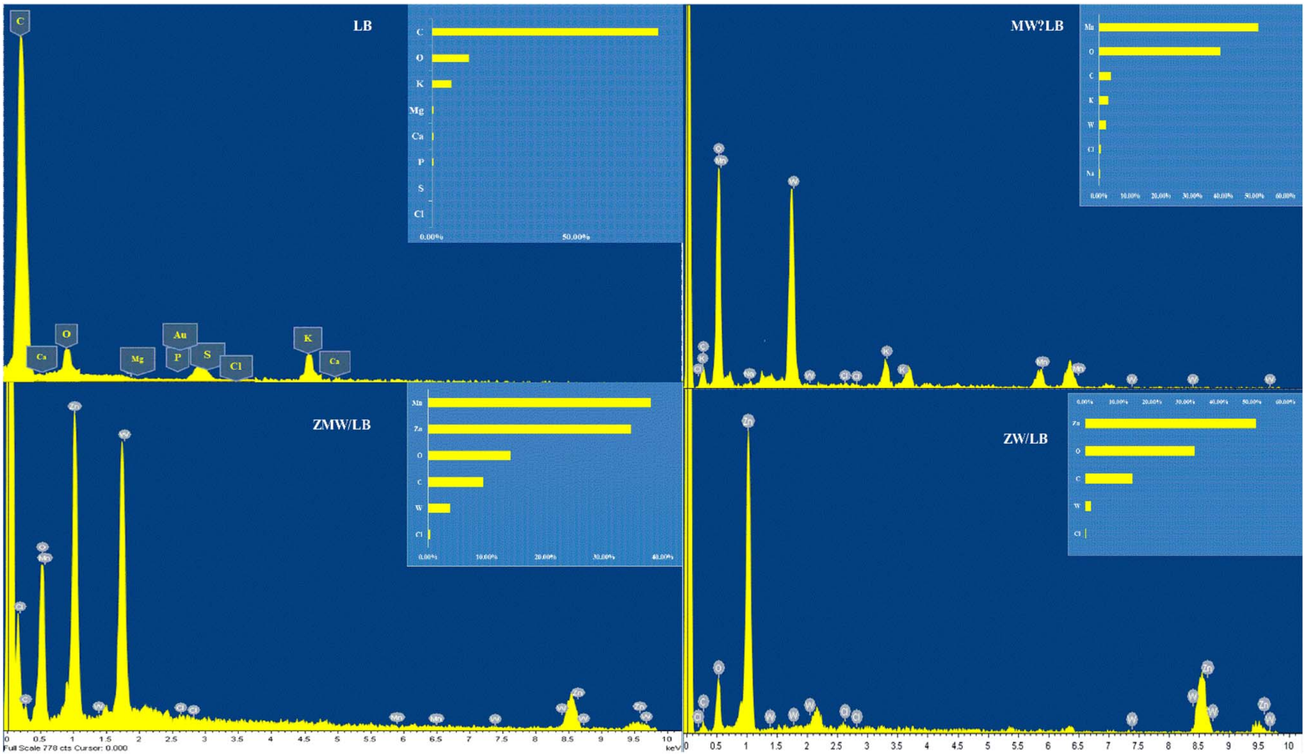

Fig. 5 EDX for LB, MW/LB, ZW/LB, and ZMW/LB.

nature of EDX analysis, gold coating, and matrix effects. A direct comparison between the mono- and bimetallic systems reveals clear differences in elemental distribution. While both MW/LB and ZW/LB composites confirm the successful incorporation of their respective metal tungstates, the bimetallic ZMW/LB exhibits a more balanced and homogeneous elemental composition. The nearly equivalent atomic ratios of Mn and W, along with the simultaneous presence of Zn, suggest the formation of a true bimetallic $Zn_xMn_{1-x}WO_4$ solid solution rather than a physical mixture of individual phases. This uniform elemental integration is expected to enhance the physicochemical properties of the composite through synergistic interactions between Zn and Mn species.

3.1.6 BET/BJH – surface area and porosity. The textural characteristics of MW/LB, ZW/LB, and ZMW/LB were examined using nitrogen adsorption–desorption isotherms recorded at 77 K, and the corresponding results are presented in Table 1 and Fig. 6. Nitrogen physisorption analysis revealed a pronounced enhancement in the textural properties of ZMW/LB compared with mono-metal counterparts. The BET surface area increased from 9.832 $m^2 g^{-1}$ for MW/LB and 26.942 $m^2 g^{-1}$ for ZW/LB to 31.259 $m^2 g^{-1}$ for the bimetallic composite. BJH analysis showed that all composites exhibited mesoporous structures with comparable pore diameters (3.077–3.426 nm), indicating that the biochar pore framework was preserved after metal tungstate incorporation.

The nitrogen adsorption–desorption isotherms of all samples correspond to type IV isotherms, characteristic of mesoporous materials.[52] Furthermore, Langmuir surface area analysis indicated enhanced monolayer adsorption capacity, with ZMW/LB exhibiting the highest surface area (360.143 $m^2 g^{-1}$), followed by ZW/LB (297.065 $m^2 g^{-1}$) and MW/LB (137.585 $m^2 g^{-1}$). Langmuir surface area values were significantly higher than BET values, which is commonly observed due to differences in the theoretical assumptions of monolayer adsorption. However, BET results are considered more representative of the actual accessible surface area.

Table 1 A summary of the N_2 adsorption–desorption isotherm study that used BET, BJH, and Langmuir methods

The physisorption property data		MW/LB	ZW/LB	ZMW/LB
BET summary	Specific surface area ($m^2 g^{-1}$)	9.832	26.942	31.259
BJH adsorption	Surface area ($m^2 g^{-1}$)	13.429	30.318	32.245
Desorption	Pore volume ($cm^3 g^{-1}$)	0.068	0.163	0.107
Summary	Pore diameter (nm)	3.077	3.826	3.392
Langmuir	Surface area ($m^2 g^{-1}$)	137.585	297.065	360.143

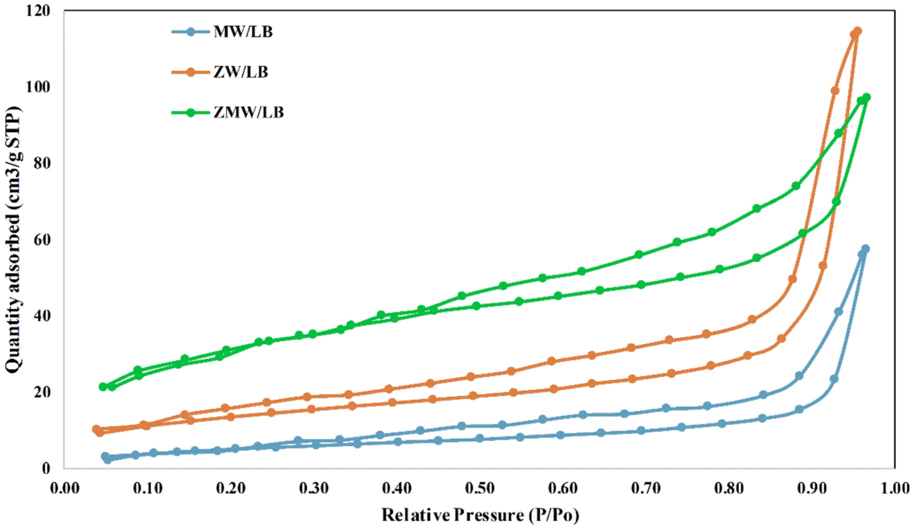

Fig. 6 The adsorption–desorption isotherms of N_2 gas at 77 K for MW/LB, ZW/LB, and ZMW/LB.

Despite the similar pore sizes, ZMW/LB displayed a markedly higher BET and Langmuir surface area than mono-metal systems, confirming that the enhanced textural properties arise from improved dispersion and synergistic interaction of Mn and Zn tungstate species rather than pore enlargement. These results confirm that co-synthesis effectively regulates particle growth and pore architecture, yielding superior adsorption–relevant properties.

The improved dispersion and reduced particle aggregation in the bimetallic ZMW/LB composite contribute to a higher specific surface area compared to the monometallic systems. In contrast, partial pore blocking and particle clustering in $MnWO_4$/biochar and $ZnWO_4$/biochar may limit surface accessibility. The preservation of the porous biochar structure in the bimetallic system, as evidenced by FESEM, supports the enhanced textural properties obtained from nitrogen adsorption–desorption measurements.

3.1.7 ICP-OES analysis. The bulk elemental composition of the bimetallic composite was quantitatively determined using ICP-OES,[53] and the results are presented in Table 2. The measured concentrations of Mn and Zn were 30 270 and 4029 µg L^{-1}, respectively, indicating that Mn is the dominant metal species in the composite. At the same time, Zn is present in a lower proportion. Based on molar calculations, the composition of the material was determined to be $Zn_{0\cdot10}Mn_{0\cdot90}(WO_4)$/LB, confirming that Zn is incorporated as a partial substituent within the $MnWO_4$ lattice rather than forming a separate phase. This finding is consistent with the XRD results, which showed peak shifts indicative of lattice distortion and solid solution formation. The difference in Zn and Mn incorporation can be attributed to their relative precursor concentrations and possible differences in nucleation and growth kinetics during hydrothermal synthesis. The lower Zn content suggests limited substitution efficiency, with Zn^{2+} ions occupying a fraction of the Mn^{2+} lattice sites, generating structural defects and heterogeneity within the crystal framework. Such partial substitution plays a critical role in tuning the composite's physicochemical properties. The presence of Zn in the $MnWO_4$ structure is expected to induce lattice distortion, modify surface charge distribution, and create additional active sites. These changes are beneficial for adsorption performance, as they enhance surface reactivity and promote stronger interactions with dye molecules.

3.2 Correlation and comparative discussion

A comprehensive physicochemical characterization of the synthesized composites was carried out using XRD, FTIR, EDX, FESEM, BET, and ICP-OES to establish a clear structure property relationship. XRD patterns confirmed the successful formation of MW/LB and ZW/LB phases in the monometallic systems, while the bimetallic ZMW/LB exhibited slight peak shifts, indicative of lattice distortion and the formation of a Zn_x-$Mn_{1-x}WO_4$ solid solution. This observation confirms the incorporation of both metal ions into a unified crystalline framework rather than the coexistence of separate phases. FTIR analysis further supported these findings by revealing

Table 2 ICP-OES elemental composition of $Zn_xMn_{x-1}(WO_4)$/LB composite

Element	Wavelength (nm)	Concentration (µg mL^{-1})	Molar concentration (mol L^{-1})	Mole fraction
Mn	257.610	30 270	5.51×10^{-4}	0.90
Zn	213.857	4029	6.16×10^{-5}	0.10

characteristic metal–oxygen vibrations (M–O and W–O), alongside oxygen-containing functional groups (–OH and –COOH) associated with the biochar matrix. These functional groups serve as active sites for both metal anchoring and subsequent adsorption interactions. Elemental analysis by EDX confirmed the presence of C, O, Mn, Zn, and W; however, due to its surface-sensitive nature, ICP-OES was employed for bulk quantification. The ICP results verified the successful incorporation of Zn and Mn within the bimetallic structure and confirmed the expected $Zn_{0.1}Mn_{0.9}WO_4$ stoichiometry, indicating the formation of a true bimetallic system. Morphological evaluation *via* FESEM revealed distinct differences between mono- and bimetallic composites. The monometallic samples exhibited noticeable particle aggregation, whereas the ZMW/LB composite showed smaller, well-dispersed nanoparticles with reduced agglomeration. This improved dispersion is attributed to the synergistic interaction between Zn and Mn, which regulates nucleation and suppresses excessive crystal growth. These observations are consistent with BET analysis, where the bimetallic composite demonstrated a higher specific surface area and improved pore accessibility.

These structural and textural enhancements directly govern the adsorption performance of the composites. The ZMW/LB composite exhibited superior removal efficiency toward aniline blue, which can be attributed to the increased density of accessible active sites, enhanced surface reactivity, and improved mass transfer facilitated by its porous structure. In contrast, aggregation in monometallic composites limits active site accessibility, resulting in lower adsorption efficiency. Overall, the combined results from structural, compositional, morphological, and textural analyses demonstrate that bimetallic engineering significantly enhances the physicochemical properties of biochar-based composites. The synergistic effect between Zn and Mn improves particle dispersion, increases surface area, and optimizes active site availability, thereby leading to enhanced adsorption performance. These findings highlight the effectiveness of bimetallic modification as a rational strategy for designing high-performance adsorbents for environmental remediation applications.

3.3 Adsorption properties

3.3.1 Effect of pH and its relation to pH_{pzc}. The pH of the solution significantly influences the adsorption of AB onto MW/LB, ZW/LB, and ZMW/LB composites because it controls both the adsorbent's surface charge and the dye's ionization state. The removal efficiency arises considerably from pH 2 to around pH 5–6, peaks in this range, and then gradually decreases at higher pH values, as seen in Fig. 7. This behavior allows a clear interpretation of the composites' point of zero charge (pH_{pzc}). Plots of ΔpH (pH_{final} − $pH_{initial}$) *vs.* initial pH were used to calculate the pH_{pzc} values. $\Delta pH = 0$ is the point that represents the pH_{pzc}. For MW/LB, ZW/LB, and ZMW/LB, the resultant pH_{pzc} values were around 8.2, 6.8, and 8.66, respectively (Fig. 8). At pH values above pH_{pzc}, the adsorbent's surface becomes negatively charged, while at pH values below pH_{pzc}, the surface is positively charged. For all composites, the surfaces are positively charged at the optimum pH of 5, which is lower than the pH_{pzc}, promoting strong electrostatic attraction with the anionic form of aniline blue, which leads to the maximum adsorption efficiency for all materials.

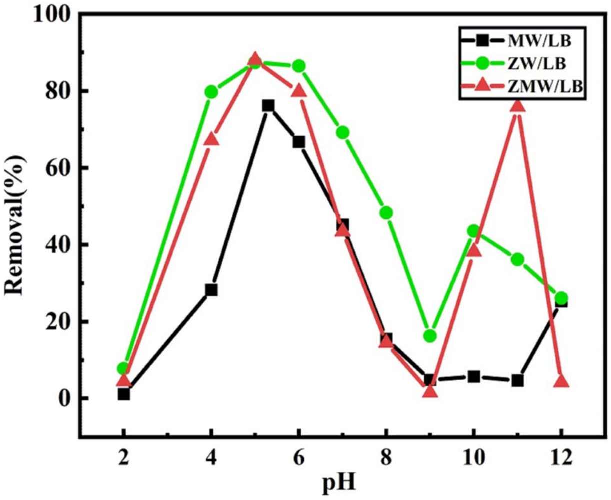

Fig. 7 Optimum pH for MW/LB, ZW/LB, and ZMW/LB.

At highly acidic conditions (pH 2–3), although the surface remains positively charged, the adsorption efficiency is relatively low. This can be explained by the competition for the available adsorption sites between the increased H^+ ions concentrations, with dye molecules, which restricts the adsorption process. When the pH rises over pH_{pzc}, the surface of adsorbent and the anionic dye molecules experience electrostatic repulsion because the surface charge becomes negative. The presence of OH^- ions under alkaline conditions may cause additional competition for active sites, resulting a decrease in adsorption effectiveness. Slight differences in adsorption behavior among the composites can be attributed to variations in their pH_{pzc} values.[54] ZW/LB, having a lower pH_{pzc}, exhibits relatively lower positive surface charge at pH 5 compared to MW/LB and ZMW/LB. In contrast, the improved performance of ZMW/LB indicates a synergistic effect between Zn and Mn species, which enhances surface characteristics and increases the active adsorption sites availability. Overall, electrostatic interactions, which are strongly influenced by the association between solution pH, adsorbent pH_{pzc}, and the ionic character of the dye, control the adsorption process.

3.3.2 Contact time effect. Fig. 9A, influence the contact time effect of AB adsorption onto MW/LB, ZW/LB, and ZMW/LB composites. All adsorbents exhibit a gradual approach to equilibrium, followed by rapid initial uptake, which is due to adsorption profiles. In the early stage (0–10 min), adsorption capacity (q_t) increases sharply, particularly for ZW/LB and ZMW/LB, where q_t rises instantly to about 75–80 mg g^{-1}. This quick increase in adsorption is caused by the significant concentration difference between the dye molecules and the adsorbent surface, as well as the amount of accessible active sites on the adsorbents' external surface. As contact duration rises (10–60 min), the adsorption rate decreases due to the start of diffusion-

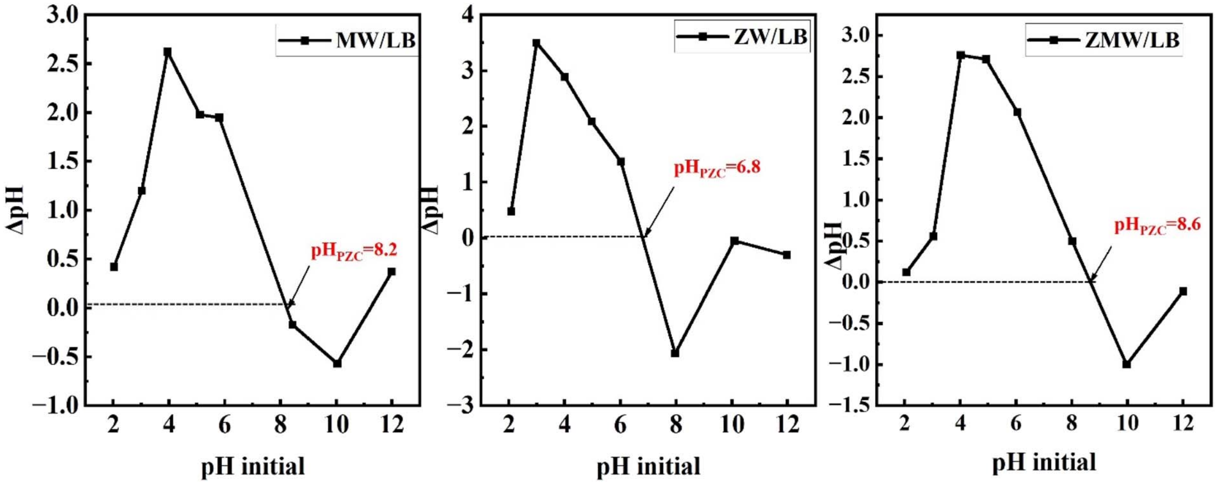

Fig. 8 pH_{pzc} for MW/LB, ZW/LB, and ZMW/LB.

controlled processes and occupation of more active sites. During this phase, dye molecules gradually penetrate the pore structure of the composites, leading to a slower rise in q_t. For all composites, equilibrium is nearly accomplished during extended contact times (≥90 min), with only minor increases in adsorption capacity. The equilibrium adsorption capacities are approximately: 80 mg g^{-1} for MW/LB, 88–90 mg g^{-1} for ZW/LB, and 89–91 mg g^{-1} for ZMW/LB. Among composites, ZW/LB and ZMW/LB, compared to MW/LB shows a better performance, due to better dispersion of metal tungstate phases on the biochar matrix, which confirms enhanced surface activity and improved availability of adsorption sites.[55] The adsorption process involves surface adsorption followed by intraparticle diffusion, and the equilibrium time is around 90–120 minutes, in accordance with the initial fast adsorption followed by a plateau behavior. The observed adsorption behavior indicates the

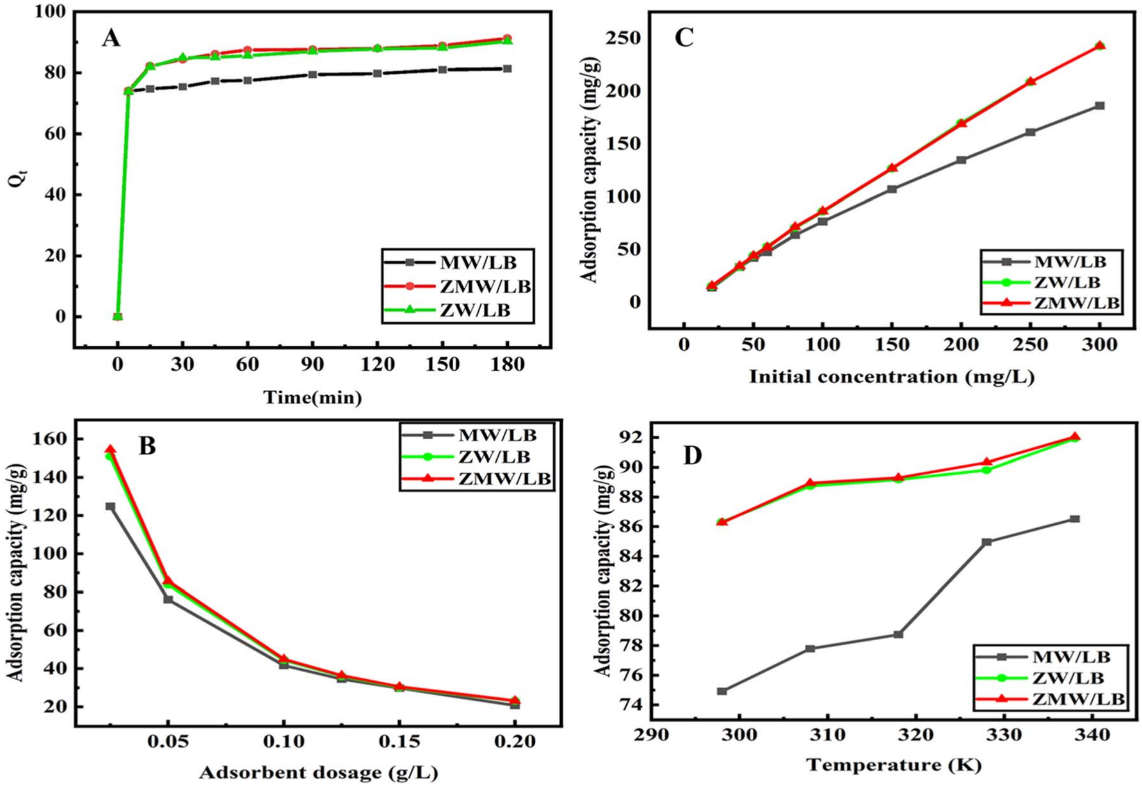

Fig. 9 (A) Impact of contact time on the adsorption of AB onto the MW/LB, ZW/LB, and ZMW/LB at 25 °C; (B) the influence of adsorbent dosage from 0.025–0.20 on AB adsorption onto the MW/LB, ZW/LB, and ZMW/LB, (C) the effect of initial concentration of AB from 25 to 300 mg L^{-1}, and (D) temperatures effects the adsorption of AB onto the MW/LB, ZW/LB, and ZMW/LB.

efficiency of the prepared composites for rapid dye removal by demonstrating that surface interactions initially control the process and are subsequently governed by diffusion into internal pores, with equilibrium achieved within a relatively short time. These findings led to the selection of 120 min as the optimum contact time for subsequent adsorption experiments to guarantee complete equilibrium.

3.3.3 Adsorbent dosage effect. Fig. 9B and S2 illustrates the effect of adsorbent dosage on the removal of AB by MW/LB, ZW/LB, and ZMW/LB composites. The decline of the adsorption capacity per unit mass (q_e, mg g^{-1}) for all composites, and an increase in the total dye removal efficiency occur when the adsorbent dose was increased from (0.025–0.20 g L^{-1}). The larger functional surface area and the increased number of accessible active sites, which facilitate more frequent dye-adsorbent interactions, are responsible for the enhancement in removal efficiency at higher doses.[56,57] Conversely, the reduction in q_e with increasing dosage arises from the distribution of a fixed amount of dye over a greater number of adsorption sites, resulting in partial underutilization. At higher adsorbent concentrations, particle aggregation can limit the accessible surface area and block active sites, further decreasing the adsorption capacity per gram. This effect is compounded by site overlapping and a reduced driving force for mass transfer. Among the composites, ZMW/LB, when compared to MW/LB and ZW/LB, consistently displayed superior adsorption performance across all dosages. As confirmed by BET, FESEM, and ICP analyses, this performance improvement is ascribed to synergistic interactions between Zn and Mn species, which increase surface heterogeneity and the density of active adsorption sites. With the goal of balancing high removal efficiency with efficient adsorbent usage, an optimal adsorbent dosage of 0.10–0.15 g L^{-1} was chosen for subsequent experiments.

3.3.4 Initial dye concentration effect. Fig. 9C demonstrate how the initial concentration of AB influences the adsorption performance of MW/LB, ZW/LB, and ZMW/LB composites. The equilibrium adsorption capacity (q_e, mg g^{-1}) for all composites steadily rose with an increase in the initial concentration of the dye. The increasing pushing force for mass transfer at higher dye concentrations is the primary cause of this trend. Adsorption capacity decreased at lower concentrations of dye since there are fewer dye molecules than there are active sites on the adsorbent surface. More dye molecules can occupy active sites as concentration rises, increasing adsorption.[58] In particular, the bimetallic ZMW/LB composite, the nearly linear rise in q_e within the studied range suggests that the adsorption sites were not saturated, confirming a strong adsorption potential and abundant accessible active sites. Among the composites, ZMW/LB continuously demonstrated the highest adsorption capacity, followed by ZW/LB, whereas MW/LB indicated relatively lower performance, as shown in Fig. S3. ZMW/LB demonstrated superior performance due to synergistic interactions between Zn and Mn species, which create a heterogeneous surface with a greater density of active sites and improved adsorption affinity. The performance difference between ZMW/LB and ZW/LB is minimal at lower dye concentrations, indicating adsorption at easily accessible surface sites. However, at higher concentrations, the bimetallic composite exhibits greater utilization of internal pores and more efficient intraparticle diffusion, underscoring its structural advantage. These findings are consistent with BET and ICP analyses, which confirm a higher density of active, heterogeneous adsorption sites in ZMW/LB, thereby explaining its enhanced adsorption efficiency.

3.3.5 Temperature effect. The effect of temperature on AB adsorption by MW/LB, ZW/LB, and ZMW/LB is shown in Fig. 9D. All composites exhibit a consistent increase in the removal efficiency when the temperature is varied from 298 to 338 K, which confirms that an endothermic mechanism was responsible for adsorption. More adsorption is observed at higher temperatures, thereby enhancing the interaction between dye molecules and the adsorbent surface. Among the studied materials, ZMW/LB outperformed MW/LB in terms of removal efficiency through the entire temperature range, followed by ZW/LB. This trend further supports the synergistic effect of Zn and Mn, which increases surface reactivity and the availability of active sites.[59] The increased mobility of dye molecules, which accelerated diffusion from the bulk solution to the adsorbent surface and improves overall mass transfer and adsorption efficiency, is responsible for the enhanced adsorption at higher temperatures.

3.4 Adsorption in deionized water (DIW)

3.4.1 Kinetic analysis in DIW. The adsorption kinetics of aniline blue adsorption (100 mg L^{-1}) onto MW/LB, ZW/LB, and ZMW/LB composites were assessed by applying the pseudo-first-order (PFO), pseudo-second-order (PSO), and intraparticle diffusion (IPD) models to better understand the rate and the mechanism of the adsorption process (Fig. 10 and Table 3).

The PFO model, which is expressed by eqn (7), makes the assumption that the adsorption rate is proportional to the number of unoccupied sites.[60]

$$q_t = q_e(1 - e^{-K_1 t}) \tag{7}$$

where q_t and q_e (mg g^{-1}) are the adsorption capacities at time t and at equilibrium, respectively, and k_1 (min^{-1}) is the rate constant. The model yielded equilibrium capacities of 78.32, 86.37, and 87.03 mg g^{-1} for MW/LB, ZW/LB, and ZMW/LB, respectively, with strong correlation values ($R^2 = 0.991$–0.992). Nevertheless, the relatively higher error values (SSE = 122.12–206.16 and $\chi^2 = 1.508$–2.283) indicate that the PFO model does not adequately describe the overall adsorption behavior, particularly for the Zn-containing composites.

In contrast, the PSO model, as described in eqn (8), offers a more realistic interpretation of the data found by experiments, which assumes that the adsorption is controlled by chemisorption involving electron sharing or exchange between adsorbent and adsorbate.[61]

$$q_t = \frac{{q_e}^2 k_2 t}{1 + q_e k_2 t} \tag{8}$$

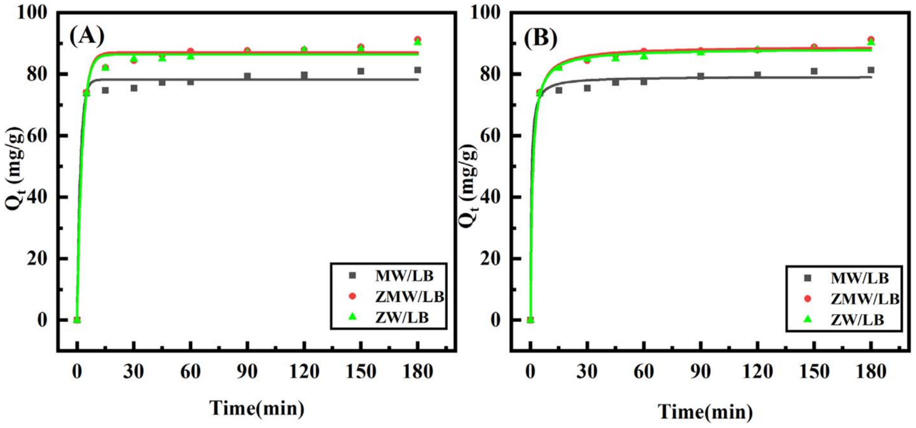

Fig. 10 (A) Pseudo-first-order and (B) Pseudo-second-order models for the adsorption of AB dye DIW solution on the surfaces of MW/LB, ZW/LB and ZMW/LB composite.

where k_2 (g mg^{-1} min^{-1}) is the rate constant. For MW/LB, ZW/LB, and ZMW/LB, the calculated equilibrium capacities were (79.23, 88.23, and 89.00 mg g^{-1}), respectively.

In comparison to the PFO model, the PSO model provided a better fit to the experimental data, with higher correlation coefficients (R^2 = 0.994–0.998) and significantly lower error values (SSE = 46.40–63.82 and χ^2 = 0.531–0.798). This indicates that the PSO model offers a more accurate representation of the adsorption kinetics. However, it should be emphasized that the applicability of the PSO model does not necessarily imply that chemisorption is the dominant mechanism. Kinetic models are primarily mathematical representations and cannot independently confirm the nature of adsorption interactions. Therefore, the adsorption mechanism is more appropriately interpreted as a combination of processes, including electrostatic attraction, surface complexation, hydrogen bonding, and π–π interactions. This interpretation is supported by FTIR spectral changes and the heterogeneous surface characteristics observed in BET and FESEM analyses.

The intra-particle diffusion model (IPD), as described in eqn (9), was used to gain extra insight into the rate-controlling mechanism.[62]

$$q_t = k_{\mathrm{id}} t^{1/2} + C \tag{9}$$

where C is the thickness of the boundary layer, and k_{id} (mg g^{-1} min$^{-1/2}$) is the rate constant.

The intra-particle diffusion (IPD) model was further applied to investigate diffusion mechanisms. The plots in Fig S4 of q_t *versus* $t^{1/2}$ exhibited multilinear behavior, indicating that adsorption proceeds through multiple stages: (i) rapid external surface adsorption, (ii) gradual intra-particle diffusion, and (iii) equilibrium stage. The fact that the plots do not pass through the origin ($C \neq 0$) confirms that intra-particle diffusion is not the sole rate-controlling step and that boundary layer diffusion also contributes significantly.

Additional analysis of the IPD variables demonstrated that ZMW/LB exhibited the highest R^2 (0.994), and lowest SSE (1.78) and χ^2 (0.021), ZW/LB also displayed significant fitting (R^2 =

Table 3 Kinetic parameter for the adsorption of 100 mg per L aniline blue dye on the surfaces of MW/LB, ZW/LB and ZMW/LB in DIW

Isotherm model	Parameters	MW/LB	ZW/LB	ZMW/LB
Pseudo-first-order	$Q_{\max}$ (mg g^{-1})	81.326	90.251	91.247
	K_1 (min^{-1})	0.576	0.381	0.376
	$Q_{(\mathrm{calc})}$ (mg g^{-1})	78.319	86.373	87.028
	R^2	0.991	0.992	0.991
	SSE	122.12	173.29	206.16
	X^2	1.508	1.940	2.283
Pseudo-second-order	K_2 (g mg^{-1} min^{-1})	0.027	0.011	0.010
	$Q_{(\mathrm{calc})}$ (mg g^{-1})	79.231	88.234	89.003
	R^2	0.994	0.998	0.997
	SSE	63.82	46.40	52.23
	X^2	0.798	0.531	0.591
Intra-particle diffusion	k_{id} (mg g^{-1} min$^{-1/2}$)	0.703	1.113	1.172
	C (mg g^{-1})	72.19	75.99	76.13
	R^2	0.978	0.991	0.994
	SSE	3.41	2.12	1.78
	X^2	0.043	0.026	0.021

0.991, SSE = 2.12, $\chi^2 = 0.026$), and MW/LB demonstrated comparatively lower accuracy ($R^2 = 0.978$, SSE = 3.41, $\chi^2 = 0.043$). Higher intercept values (C) for ZW/LB and ZMW/LB indicate faster initial adsorption and more noticeable boundary-layer effects. Furthermore, the improved dispersion of metal tungstate particles on the biochar matrix, which enhances access to active sites, is responsible for the larger k_{id} value for ZMW/LB, suggesting accelerated diffusion of dye molecules within its porous network.

Overall, the adsorption process follows a multi-step mechanism involving surface interactions and diffusion processes, with ZMW/LB exhibiting enhanced performance due to improved active site availability and pore accessibility.

3.4.2 Isotherm analysis in DIW.

The Langmuir and Freundlich isotherm models were used to analyze equilibrium adsorption behavior of aniline blue onto MW/LB, ZW/LB, and ZMW/LB composites[63] (Fig. 11 and Table 4).

The Langmuir model assumes monolayer adsorption on relatively uniform active sites and is expressed as in eqn (10):[63]

$$q_{\mathrm{e}} = \frac{q_{\max} K_{\mathrm{L}} C_{\mathrm{e}}}{1 + K_{\mathrm{L}} C_{\mathrm{e}}} \tag{10}$$

where K_{L} is the Langmuir constant associated with the affinity of the adsorbent surface, and C_{e} (mg L^{-1}) is the dye's equilibrium concentration.

The model showed good agreement with experimental data ($R^2 = 0.982$–0.987) and relatively lower error values SSE (1702–21 603) and χ^2 (12.6–107), indicating a tendency toward monolayer adsorption. The calculated maximum adsorption capacities ($Q_{\max}$) were 276.90, 597.99, and 586.97 mg g^{-1} for MW/LB, ZW/LB, and ZMW/LB, respectively. The enhanced performance of Zn-containing composites is attributed to increased surface reactivity and improved accessibility of active sites.

The Freundlich model as in eqn (11):[64]

$$q_{\mathrm{e}} = k_{\mathrm{f}} C_{\mathrm{e}}^{\frac{1}{n}} \tag{11}$$

where the adsorption intensity is represented by $1/n$, and the capacity of adsorption is represented by K_{f}. The Freundlich model also described the adsorption behavior ($R^2 = 0.975$–0.984), indicating surface heterogeneity and the presence of adsorption sites with varying energies. The obtained K_{f} values (10.56–11.27 mg g^{-1} (L mg^{-1})$^{1/n}$) demonstrate a significant affinity of the adsorbents toward aniline blue, while $1/n$ values (0.608–0.775) show good adsorption with moderate surface heterogeneity. The obtained parameters suggest favorable adsorption and non-ideal surface behavior. However, higher SSE and χ^2 values compared to the Langmuir model indicate a less accurate fit.

To further assess adsorption favorability,[65] the dimensionless separation factor (R_{L}) was calculated by using eqn (12):

$$R_{\mathrm{L}} = \frac{1}{1 + K_{\mathrm{L}} C_{\mathrm{e}}} \tag{12}$$

The separation factor ($0 < R_{\mathrm{L}} < 1$) confirms that adsorption is favorable for all composites. Moreover, the gradual decrease in R_{L} with increasing initial dye concentration reflects a stronger driving force and enhanced adsorbate–adsorbent interactions at higher concentrations.

Overall, the results suggest that adsorption predominantly follows Langmuir-type behavior with contributions from heterogeneous surface interactions, including electrostatic attraction, π–π stacking with the biochar matrix, and surface complexation with metal–oxygen functional groups.

3.4.3 Thermodynamic analysis in DIW.

Van't Hoff plots (Fig. 12 and Table 5) were employed to evaluate the impact of temperature on the adsorption of aniline blue onto MW/LB, ZW/LB, and ZMW/LB composites, with the findings displayed in Table 5. The following equations were employed to determine the thermodynamic parameters, such as enthalpy change ($\Delta H°$), entropy change ($\Delta S°$), and Gibbs free energy change ($\Delta G°$) (eqn (13)–(15)):[66,67]

$$K_{\mathrm{d}} = \frac{q_{\mathrm{e}}}{C_{\mathrm{e}}} \tag{13}$$

$$\ln K_{\mathrm{d}} = \frac{\Delta H^{\circ}}{RT} - \frac{\Delta S}{R} \tag{14}$$

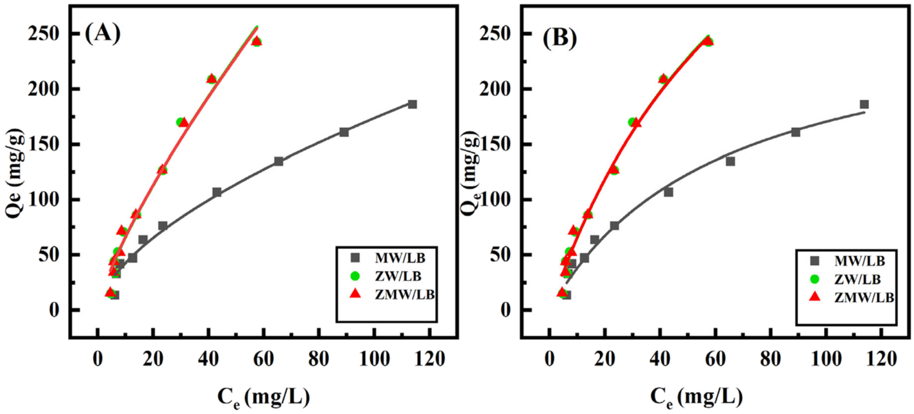

Fig. 11 Adsorption isotherms plot for the adsorption of AB dye (A) Freundlich adsorption isotherm, (B) Langmuir adsorption isotherm onto MW/LB, ZW/LB and ZMW/LB adsorbents.

Table 4 Data of Langmuir and Freundlich isotherms adsorption of aniline blue dye on the surfaces of MW/LB, ZW/LB and ZMW/LB in DIW

Isotherm model	Parameters	MW/LB	ZW/LB	ZMW/LB
Langmuir	Q_{max} (mg g^{-1})	276.899	597.985	586.969
	K_L (L mg^{-1})	0.016	0.012	0.014
	R^2	0.982	0.985	0.987
	R_L	0.862–0.385	0.893–0.455	0.877–0.416
	SSE	21 603	2688	1702
	X^2	107	39.6	12.6
Freundlich	K_f (mg g^{-1}). (L mg^{-1})$^{1/n}$	10.556	11.066	11.268
	$1/n$	0.608	0.775	0.770
	R^2	0.984	0.975	0.979
	SSE	25 435	85 842	82 725
	X^2	402	1856	1624

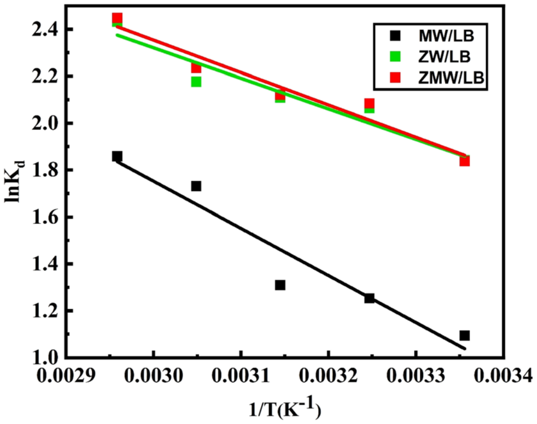

Fig. 12 Van't Hoff curve for AB dye onto MW/LB, ZW/LB and ZMW/LB adsorbents.

Table 5 Thermodynamic parameters data at different temperatures of aniline blue adsorption on MW/LB, ZW/LB and ZMW/LB in DIW

Adsorbent	T (K)	$\Delta G°$ (kJ mol^{-1})	K_d	$\Delta S°$ (J mol^{-1} K)	$\Delta H°$ (kJ mol^{-1})
MW/LB	298	−2.571	1.093	64.678	16.703
	308	−3.217	1.252		
	318	−3.864	1.309		
	328	−4.511	1.730		
	338	−5.157	1.857		
ZW/LB	298	−4.604	1.841	51.735	10.813
	308	−5.121	2.064		
	318	−5.638	2.108		
	328	−6.155	2.176		
	338	−6.673	2.432		
ZMW/LB	298	−4.613	1.837	53.999	11.477
	308	−5.152	2.084		
	318	−5.692	2.121		
	328	−6.232	2.234		
	338	−6.772	2.448		

$$\Delta G^{\circ} = -RT \ln K_d \tag{15}$$

where K_d is the adsorption distribution constant, R is the gas constant (8.314 J mol^{-1} K^{-1}), and T is the absolute temperature (K). The slope and intercept of the linear plot of ln K_d *versus* $1/T$ were utilized to calculate the enthalpy ($\Delta H°$) and entropy ($\Delta S°$). The endothermic character of the process was confirmed by a linear relationship that was observed for all composites, which indicates that adsorption becomes more beneficial at higher temperatures. This observation aligns with the positive $\Delta H°$ values (10.813–16.703 kJ mol^{-1}), which suggest that heat energy promotes diffusion into internal pores and enhances dye mobility to facilitate adsorption. The adsorption is spontaneous and thermodynamically effective, particularly at elevated temperatures, as evidenced by the negative $\Delta G°$ values across the studied temperature range (298–338 K), which become increasingly negative with temperature. The increased randomness at the interface of solid–liquid is demonstrated by positive $\Delta S°$ values (51.735–64.678 J mol^{-1} K^{-1}), likely due to the water molecules displacement and rearrangement of the structure on the adsorbent surface during dye uptake. Among the composites, ZMW/LB and ZW/LB exhibited more negative $\Delta G°$ values than MW/LB, reflecting stronger adsorption affinity and enhanced thermodynamic favorability, which can be attributed to the synergistic interactions between Zn and Mn species and increased surface activity. Overall, the thermodynamic study consistent with the Van't Hoff plot and the determined thermodynamic parameters confirms that the adsorption of aniline blue is spontaneous, endothermic, and entropy-driven.

3.5 Adsorption in simulated wastewater (SWW)

To evaluate the performance of the developed composites under realistic conditions, adsorption experiments were conducted in simulated wastewater (SWW) containing common competing ions (Na^+, Ca^{2+}, and Mg^{2+}). The effects of pH, adsorbent dosage, contact time, and temperature were investigated. The overall trends observed in SWW were consistent with those in deionized water, indicating that the fundamental adsorption mechanism remains largely unchanged, as shown in Fig S5 and S6.

The optimal pH remained around 5, confirming that electrostatic interactions play a dominant role even in complex matrices. Increasing adsorbent dosage enhanced removal efficiency due to the greater availability of active sites, although the effect was less pronounced compared to DIW due to partial site occupation by competing ions. A slight reduction in adsorption performance was observed in SWW, which can be attributed to ionic competition and electrostatic screening effects. Kinetic studies showed rapid adsorption followed by equilibrium within 90–120 min, indicating that mass transfer processes are not significantly hindered. Temperature-dependent results confirmed that adsorption remains endothermic under SWW conditions.[68–70] These findings demonstrate that the developed composites maintain high efficiency and stability in complex systems, supporting their potential applicability in real wastewater treatment.

3.5.1 Kinetic analysis. The adsorption kinetics in simulated wastewater were analyzed using PFO, PSO, and IPD models (Table 6 and Fig. 13). Both PFO and PSO models showed good agreement with experimental data; however, the PSO model exhibited higher correlation coefficients ($R^2 = 0.991$–0.998) and lower error values (SSE = 6.03–12.74; $\chi^2 = 0.071$–0.152), indicating superior fitting accuracy. Compared to DIW, the differences between models were less pronounced, suggesting increased complexity of adsorption under multicomponent conditions. This behavior reflects the influence of competing ions on diffusion pathways and active site accessibility.[68] The IPD model further confirmed a multi-step adsorption mechanism. The k_{id} values (0.49–0.63 mg g^{-1} min$^{1/2}$) indicate relatively fast diffusion, while the non-zero intercept values ($C \neq 0$) confirm that intra-particle diffusion is not the sole rate-limiting step. Instead, adsorption is governed by a combination of surface interactions, boundary layer diffusion, and intra-particle diffusion,[70] as shown in Fig. S7. Overall, the kinetic analysis demonstrates that adsorption proceeds *via* a multi-step mechanism, influenced by surface interactions, diffusion limitations, and ionic competition, this increase complexity in simulated wastewater.

3.5.2 Isotherm analysis. The equilibrium adsorption behavior in simulated wastewater was analyzed using Langmuir and Freundlich isotherm models (Table 7 and Fig. 13). The Langmuir model provided a better overall fit for MW/LB and ZW/LB, with relatively higher R^2 values (0.972–0.977) and lower error values (SSE = 98.7–125.4; $\chi^2 = 1.45$–1.92), suggesting that adsorption predominantly occurs through monolayer coverage on energetically uniform sites.[70] In contrast, ZMW/LB exhibited a slightly better fit with the Freundlich model ($R^2 = 0.972$), indicating increased surface heterogeneity in the bimetallic system. The maximum adsorption capacities ($Q_{\max}$) decreased under SWW conditions compared to deionized water, with values of 291.43, 426.42, and 318.86 mg g^{-1} for MW/LB, ZW/LB, and ZMW/LB, respectively. This reduction reflects the effect of competing ions, which occupy active sites and reduce adsorption efficiency.[71]

The calculated separation factor ($R_{\text{L}} = 0.244$–0.312) confirms that adsorption remains favorable for all composites under simulated conditions. However, slightly higher R_{L} values compared to DIW indicate reduced adsorption affinity in the presence of ionic species. The Freundlich constants further support this observation, where variations in $1/n$ values suggest moderate surface heterogeneity and non-ideal adsorption behavior, particularly for ZMW/LB. Overall, the isotherm analysis demonstrates that adsorption remains effective in complex systems but deviates from ideal monolayer behavior due to competitive adsorption and surface heterogeneity.

3.5.3 Thermodynamic analysis. Thermodynamic parameters for aniline blue adsorption under simulated wastewater conditions were calculated using Van't Hoff analysis (Table S3 and Fig. S8). The positive $\Delta H°$ values (12.658–16.591 kJ mol^{-1}) indicate that the adsorption process remains endothermic in the presence of competing ions, suggesting that elevated temperatures enhance dye mobility and facilitate adsorption.[71] The magnitude of $\Delta H°$ falls within the range typically associated with physical adsorption or weak chemical interactions, supporting the conclusion that adsorption is not purely chemisorptive. Negative $\Delta G°$ values across the studied temperature range confirm that the adsorption process is spontaneous, with increasing negativity at higher temperatures indicating enhanced thermodynamic favorability. Notably, ZW/LB exhibited the most negative $\Delta G°$ values, consistent with its superior adsorption performance under simulated conditions. The positive $\Delta S°$ values (58.804–66.753 J mol^{-1} K) suggest increased

Table 6 Kinetic model parameters and error analysis in SWW

Isotherm model	Parameters	MW/LB	ZW/LB	ZMW/LB
Pseudo-first-order	Q_{max} (mg g^{-1})	85.713	91.007	86.831
	K_1 (min^{-1})	0.540	0.650	0.434
	$Q_{(\text{calc})}$ (mg g^{-1})	83.631	89.246	82.641
	R^2	0.996	0.997	0.982
	SSE	18.42	15.66	29.85
	X^2	0.221	0.174	0.362
Pseudo-second-order	K_2 (g mg^{-1} min^{-1})	0.024	0.041	0.012
	$Q_{(\text{calc})}$ (mg g^{-1})	84.564	89.819	83.797
	R^2	0.998	0.998	0.991
	SSE	7.12	6.03	12.74
	X^2	0.087	0.071	0.152
Intra-particle diffusion	k_{id} (mg g^{-1} min$^{-1/2}$)	0.58	0.63	0.49
	C (mg g^{-1})	77.3	84.5	72.8
	R^2	0.987	0.991	0.978
	SSE	3.21	2.74	5.62
	X^2	0.039	0.031	0.067

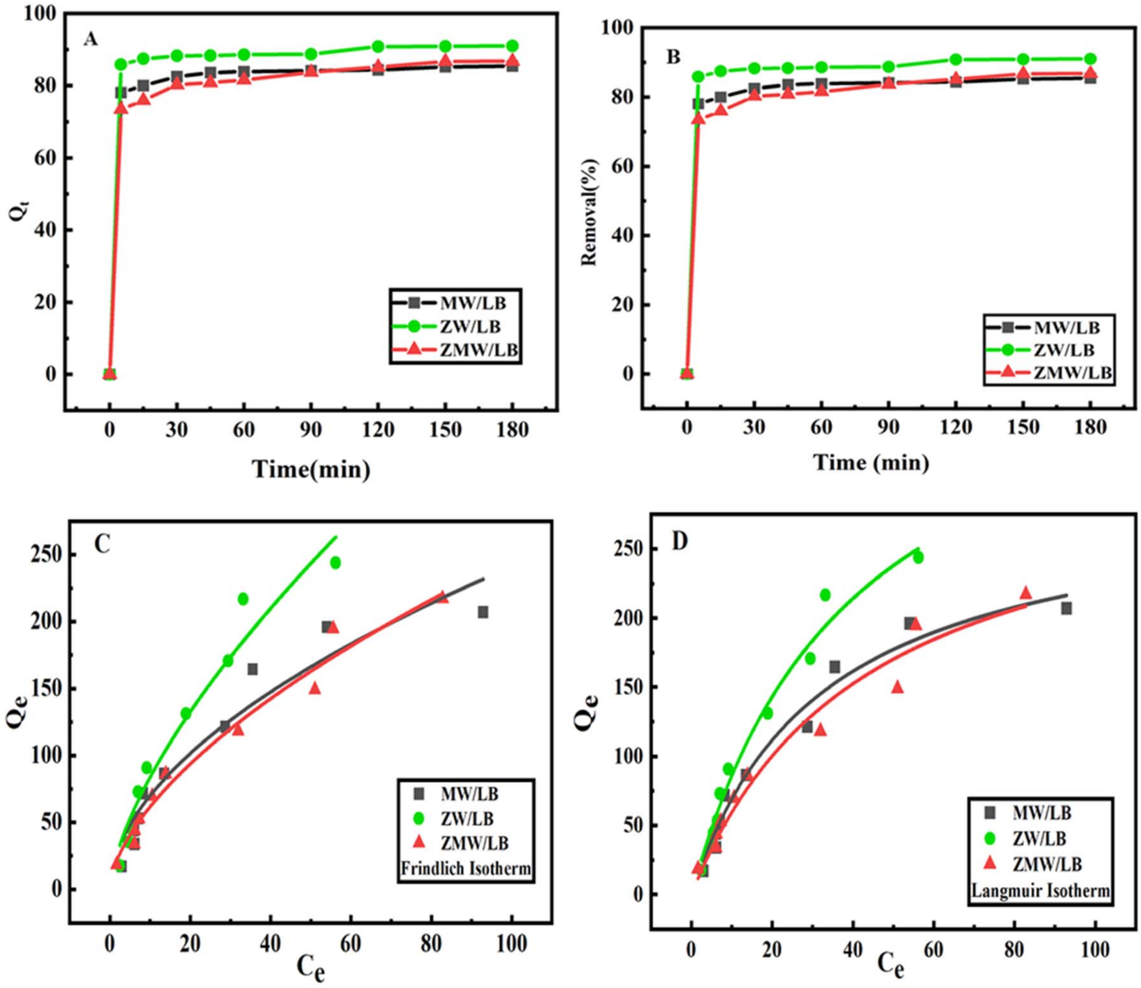

Fig. 13 Kinetic and Isotherm analysis in SWW for the adsorption of AB dye on the surfaces of MW/LB, ZW/LB and ZMW/LB composite: (A) Pseudo-first-order and (B) Pseudo-second-order models, (C) Freundlich adsorption isotherm, (D) Langmuir adsorption isotherm.

Table 7 Isotherm parameters and error analysis in SWW

Isotherm model	Parameters	MW/LB	ZW/LB	ZMW/LB
Langmuir	Q_{max} (mg g^{-1})	291.426	426.420	318.861
	K_L (L mg^{-1})	0.031	0.025	0.022
	R^2	0.972	0.977	0.963
	R_L	0.244	0.286	0.312
	SSE	125.4	98.7	142.8
	X^2	1.92	1.45	2.11
Freundlich	K_f (mg g^{-1}) (L mg^{-1})$^{1/n}$	20.268	18.205	15.363
	$1/n$	0.537	0.663	0.603
	R^2	0.926	0.956	0.972
	SSE	382.6	310.2	210.4
	X^2	4.87	3.66	2.98

randomness at the solid–liquid interface, likely due to displacement of water molecules and structural rearrangements during adsorption.

Compared to deionized water, slight variations in thermodynamic parameters were observed, reflecting the influence of ionic strength and competitive adsorption. These findings confirm that adsorption remains thermodynamically favorable under realistic conditions, although the mechanism becomes more complex.

3.6 Effect of water matrix: DIW *versus* SWW

A comparative evaluation of adsorption performance in DIW and SWW was conducted to assess the robustness of the developed composites under realistic conditions. Overall, adsorption trends in SWW closely followed those in DIW, indicating that the fundamental adsorption mechanism is largely preserved despite the presence of competing ions. In both systems, adsorption was strongly pH-dependent, with maximum removal observed at pH ≈ 5, confirming that electrostatic interactions remain dominant. However, a slight reduction in removal efficiency was observed in SWW, which can be attributed to ionic competition and electrostatic shielding by coexisting ions (Na^+, Ca^{2+}, Mg^{2+}).[68] Increasing adsorbent dosage enhanced removal efficiency in both systems due to greater availability of active sites, although the effect was less pronounced in SWW, reflecting partial site occupation and reduced accessibility.[69]

Kinetic analysis showed rapid adsorption followed by equilibrium within 90–120 min in both media, indicating that mass transfer processes are not significantly hindered by ionic strength. Nevertheless, slightly lower equilibrium capacities in SWW suggest moderate effects on diffusion and surface interactions. Thermodynamic behavior remained consistent in both systems, confirming the endothermic nature of adsorption and indicating that the process is thermodynamically stable under complex conditions.[71] Among the composites, ZW/LB exhibited the highest removal efficiency in both DIW and SWW, demonstrating superior resistance to ionic interference. In contrast, ZMW/LB, although highly effective in DIW, showed slightly greater sensitivity to competing ions, likely due to increased surface heterogeneity. MW/LB displayed lower adsorption capacity but more stable performance, suggesting stronger but fewer active binding sites. Overall, these results confirm that while competing ions slightly reduce adsorption efficiency, the developed composites maintain high performance and stability, supporting their applicability in real wastewater systems.

3.7 Practical applicability and mass balance evaluation

To evaluate the practical feasibility and scale-up potential of the developed adsorption system, a comprehensive mass balance analysis was performed using both experimentally determined equilibrium adsorption capacities (q_e) and theoretical Langmuir maximum capacities (Q_{max}). This dual approach provides a realistic assessment of adsorbent demand under actual operating conditions while also defining the theoretical performance limits of the prepared composites. The required adsorbent dosage under real conditions was estimated using equilibrium capacities as in eqn (16) according to ref. 72:

$$\text{Adsorbent dose}\left(\text{g L}^{-1}\right) = \frac{C_0}{q_e} \tag{16}$$

where C_0 is the initial dye concentration (mg L^{-1}) and q_e is the equilibrium adsorption capacity (mg g^{-1}) obtained under simulated wastewater (SWW) conditions. At an initial dye concentration of 100 mg L^{-1}, the experimentally derived q_e values were 84.56 mg g^{-1} for MW/LB, 89.82 mg g^{-1} for ZW/LB, and 83.80 mg g^{-1} for ZMW/LB. Accordingly, the calculated adsorbent dosages were 1.18, 1.11, and 1.19 g L^{-1}, respectively, corresponding approximately to (1180, 1110, and 1190 g m^{-3}) of wastewater treatment capacity. Among the tested materials, ZW/LB exhibited the lowest dosage requirement, confirming its superior adsorption efficiency under realistic conditions. The slightly higher demands for MW/LB and ZMW/LB may be attributed to variations in surface accessibility and interaction strength with the dye molecules, as illustrated in Table 8.

For comparison, theoretical dosage requirements were also estimated using Langmuir maximum adsorption capacities under ideal monolayer coverage, as in eqn (17):[73]

$$\text{Adsorbent dose}\left(\text{g L}^{-1}\right) = \frac{C_0}{Q_{max}} \tag{17}$$

Under this assumption, the required dosages at 100 mg L^{-1} were significantly lower, estimated as 0.343 g L^{-1} for MW/LB, 0.235 g L^{-1} for ZW/LB, and 0.314 g L^{-1} for ZMW/LB (equivalent to 235–343 g m^{-3}). However, these theoretical values represent idealized conditions and do not account for mass transfer limitations, incomplete site utilization, or ionic competition typically present in real wastewater systems.

A comparison between Q_{max}- and q_e-based calculations clearly demonstrates that equilibrium-derived values provide a more realistic basis for process design. While Q_{max} reflects maximum adsorption potential, q_e better captures actual system performance under operational constraints. This discrepancy highlights the importance of using experimentally validated parameters for reliable scale-up and engineering applications.[74]

When both DIW and SWW conditions were considered, the required adsorbent dosage remained relatively consistent, ranging from 1.12–1.27 g L^{-1} in DIW and 1.11–1.19 g L^{-1} in SWW. This narrow variation indicates that the presence of competing ions has minimal influence on adsorption efficiency, confirming the stability of the prepared composites in complex aqueous matrices. In practical terms, this corresponds to approximately 1.1–1.2 kg of adsorbent per m^3 of wastewater containing 100 mg L^{-1} of aniline blue.

Overall, the mass balance evaluation confirms that the developed materials are practically viable for wastewater treatment at realistic loading levels. ZW/LB consistently demonstrates the most favorable performance, combining high adsorption efficiency with the lowest material requirement. Importantly, the close agreement between DIW- and SWW-based calculations further validates the robustness of the system and its suitability for real environmental conditions. These findings bridge the gap between laboratory adsorption performance and full-scale application, providing a solid foundation for future engineering design and scale-up studies.

3.8 Cost efficiency based on adsorption capacity

To further evaluate the economic performance of the developed adsorbents, the cost per unit mass of dye removed was estimated by normalizing the adsorbent cost to the maximum adsorption capacity (Q_{max}), as illustrated in eqn (18).[75] The

Table 8 Comparison of equilibrium adsorption capacity (q_e) and estimated adsorbent dose in deionized water (DIW) and simulated wastewater (SWW) at $C_0 = 100$ mg L^{-1}

Adsorbent	q_e (DIW) (mg g^{-1})	Dose (DIW) (g L^{-1})	q_e (SWW) (mg g^{-1})	Dose (SWW) (g L^{-1})
MW/LB	79.23	1.27	84.56	1.18
ZW/LB	88.23	1.14	89.82	1.11
ZMW/LB	89.00	1.12	83.80	1.19

calculated values were approximately 145, 75, and 73 USD per kg of dye removed for MW/LB, ZW/LB, and ZMW/LB, respectively, as shown in Table 9.

$$\text{Cost efficiency} = \frac{\text{Cost of adsorbent (USD per kg adsorbent)}}{\text{Adsorption capacity(kg Dye per kg adsorbent)}} \tag{18}$$

These results indicate that, despite similar synthesis costs, the significantly higher adsorption capacities of Zn-containing composites lead to substantially improved cost efficiency.

In particular, ZMW/LB exhibited the lowest cost per unit dye removal, reflecting an optimal balance between material cost and adsorption performance, while MW/LB showed the least favorable economic performance due to its lower adsorption capacity. This analysis highlights that adsorption capacity is a key factor governing not only environmental impact but also economic feasibility, further supporting the advantage of Zn-based and bimetallic systems for practical wastewater treatment applications.

It should be noted that the cost estimation presented in this study primarily reflects the contribution of precursor materials, which represent the dominant cost factor particularly Na_2WO_4. Additional contributions from energy consumption, NaOH used in regeneration, and biochar support were considered qualitatively. Energy consumption, although relatively high at laboratory scale, is expected to decrease significantly under large-scale production due to improved process efficiency and heat integration. Similarly, NaOH consumption is distributed over multiple adsorption–desorption cycles, reducing its overall contribution to operational cost. Biochar, derived from low-cost biomass, contributes minimally to the total material cost. Therefore, the calculated cost per unit mass of dye removed represents a realistic approximation of economic performance, while acknowledging that full techno-economic evaluation would require large-scale operational data.

3.9 Structure–performance relationship

The adsorption performance of MW/LB, ZW/LB, and ZMW/LB composites was interpreted by correlating experimental adsorption results with physicochemical properties and multivariate analysis. Among the studied materials, ZW/LB exhibited the highest removal efficiency toward aniline blue, followed by ZMW/LB and MW/LB. This tendency is primarily controlled by differences in textural properties, where higher BET surface area and pore volume provide a greater number of accessible adsorption sites. MW/LB exhibits comparatively better reusability but slightly lower removal efficiency, confirming a more stable structure with fewer active sites. This trend, which is commonly observed in porous adsorbent systems, suggests a trade-off between adsorption capacity and structural durability. Kinetic analysis is well described by the pseudo-second-order model; however, this does not imply a single rate-limiting mechanism but rather reflects the combined contribution of surface interactions and diffusion processes.

Table 9 Cost Effectiveness and economic performance expressed as cost per kg dye removed

Adsorbent	$Q_{\max}$ (mg g^{-1})	Cost (USD per kg)	Cost (USD per kg dye removed) (USD per kg)
MW/LB	276.90	40	145
ZW/LB	597.99	45	75
ZMW/LB	586.97	43	73

Both Langmuir and Freundlich isotherms were supported by equilibrium data, suggesting that adsorption occurs through a combination of monolayer coverage and heterogeneous surface interactions.

Morphological and structural analyses further support these findings. FESEM images showed a porous biochar matrix coated with well-dispersed metal tungstate nanoparticles, enhancing surface roughness and facilitating dye diffusion. XRD patterns verified the crystalline phase's development, indicating structural stability of the composites. Additionally, BET analysis demonstrated that enhanced adsorption effectiveness depends on surface area and pore structure.

Overall, the results demonstrate that adsorption performance is mainly governed by the availability and accessibility of active sites, which are directly influenced by pore structure and surface area. Meanwhile, surface chemistry contributes to fine-tuning adsorption behavior under different conditions. This structure–performance relationship provides valuable insight for the rational design of efficient biochar-based adsorbents.

3.10 Mechanism of adsorption

The adsorption of aniline blue onto the synthesized composites is governed by synergistic physicochemical interactions. At pH 5, the surfaces of all composites are mostly positively charged, which promotes strong electrostatic attraction toward anionic dye molecules, enhancing rapid initial uptake. In addition, the biochar matrix provides abundant oxygen-containing functional groups (–OH and –COOH) that can form hydrogen bonds with AB molecules, thereby enhancing adsorption stability and surface affinity.[6,76]

The incorporated metal ions provide additional active sites: Mn^{2+} in MW/LB and Zn^{2+} in ZW/LB serve as Lewis acidic centers capable of coordinating with electron-rich sites of the dye. In the bimetallic ZMW/LB, the partial substitution of Mn by Zn introduces slight structural heterogeneity, enhancing the variety of surface sites. However, since ZMW/LB is predominantly Mn (90% Mn, 10% Zn), its adsorption behavior mainly reflects the characteristics of $MnWO_4$. Moreover, the aromatic framework of AB can interact with the graphitic domains of all biochar composites *via* π–π stacking, further improving adsorption capacity, as shown in Fig. 14.

The FTIR analysis before and after adsorption supports the aforementioned interaction, as shown in Fig. 15, the broad –OH band at 3200–3500 cm^{-1} shows shifts and changes in intensity post-adsorption, indicating hydrogen bonding; peaks around 1600–1650 cm^{-1} (C═C aromatic/C═O) demonstrate π–π interactions; and modifications in the 1000–1200 cm^{-1} region

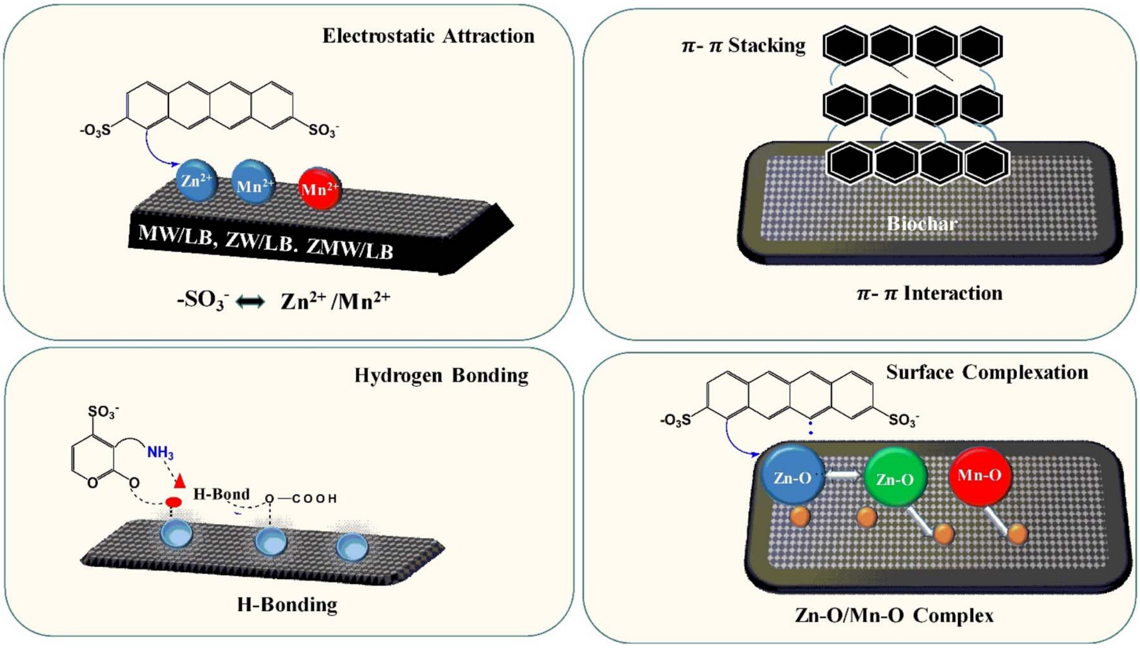

Fig. 14 Adsorption mechanisms of AB dye onto MW/LB, ZW/LB and ZMW/LB adsorbents.

(C–O stretching) signal the involvement of oxygen-containing functional groups. Slight variations in the low-wavenumber range (500–800 cm^{-1}) suggest integration interactions with metal active sites.[77] In general, adsorption on MW/LB, ZW/LB, and ZMW/LB is governed by electrostatic attraction, hydrogen bonding, π–π interactions, and metal-dye surface complexation. Variations in performance among the composites are attributed to their metal content, surface heterogeneity, and accessible active sites, as evidenced by pre-adsorption characterizations (XRD, BET, and ICP) and FTIR results. This mechanism aligns with kinetic and isotherm analyses, confirming the robustness of the proposed interactions in governing AB removal. It is important to note that no single interaction dominates the adsorption process; instead, the overall performance arises from the combined and synergistic contribution of multiple mechanisms.

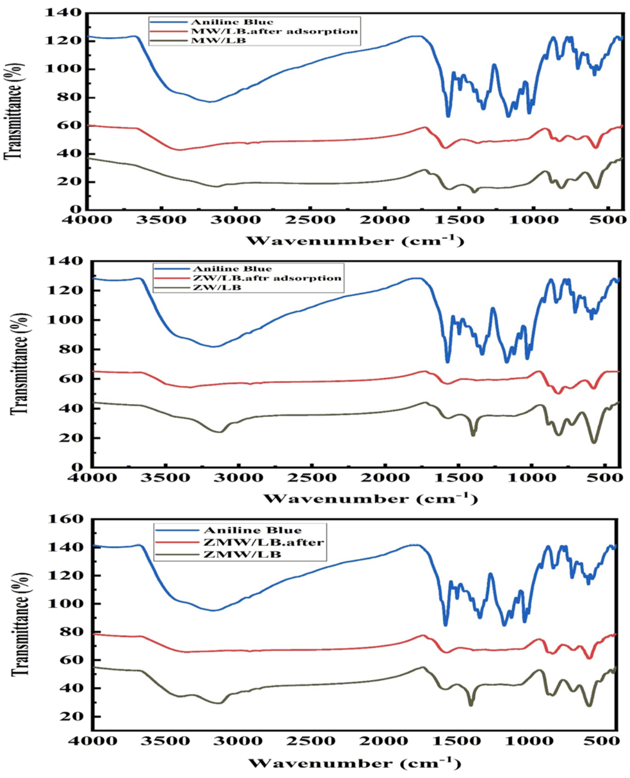

Fig. 15 FTIR for AB and prepared composites before and after adsorption.

3.11 Application in simulated wastewater: adsorption efficiency, desorption, and reusability

The practical applicability of MW/LB, ZW/LB, and ZMW/LB composites was evaluated using simulated wastewater (SWW) containing common competing ions (Na^{+}, Ca^{2+}, and Mg^{2+}) in the presence of aniline blue. All composites maintained high removal efficiencies under these complex conditions, confirming their potential for real wastewater treatment (Table 10 and Fig. 16).

However, a slight reduction in performance compared to DIW was observed, which can be attributed to ionic competition and electrostatic screening effects that limit the accessibility of active adsorption sites.[76] Among the investigated materials, ZMW/LB exhibited the highest removal efficiency in DIW (89.16% ± 0.72), while ZW/LB demonstrated the best performance in SWW (89.33% ± 1.92), indicating superior resistance to ionic interference. In contrast, MW/LB showed comparatively lower removal efficiencies (80.73% ± 1.10 in DIW and 83.07% ± 1.56 in SWW) but exhibited more stable behaviour in the

Table 10 Removal efficiency of adsorbents (MW/LB, ZW/LB, and ZMW/LB) in removing AB from DIW and SWW[a]

Composite	% removal (DIW) ± SD*	% removal (SWW) ± SD*
MW/LB	80.73 ± 1.1015	83.07 ± 1.5653
ZW/LB	87.05 ± 0.4802	89.33 ± 1.9269
ZMW/LB	89.16 ± 0.7287	85.98 ± 0.3905

[a] Each experiment was repeated three times.

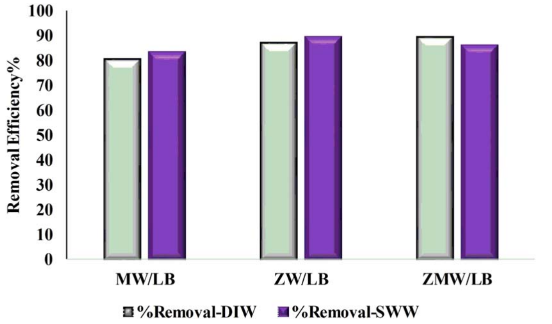

Fig. 16 Removal efficiency of adsorbents (MW/LB, ZW/LB, and ZMW/LB) for removing AB from DIW and SWW.

presence of competing ions. The slight decrease in ZMW/LB performance in SWW (85.98% ± 0.39) suggests that bimetallic systems, despite their high adsorption capacity, are more sensitive to ionic competition due to increased surface heterogeneity.

To further assess practical applicability, adsorption–desorption experiments were conducted over five successive cycles using 0.1 M NaOH as the desorbing agent (Fig. 17). All composites exhibited relatively high desorption efficiencies (75–90%), indicating that the adsorption process is largely reversible and governed predominantly by weak interactions such as electrostatic attraction, π–π interactions, and hydrogen bonding.[77]

The reusability study revealed a gradual decrease in removal efficiency across repeated cycles, commonly attributed to incomplete desorption and progressive occupation of active sites. As shown in Fig. 17, the adsorbents retained more than 95% of their initial removal efficiency after five adsorption–desorption cycles, demonstrating excellent structural stability and regeneration capability. A clear trade-off between adsorption capacity and regeneration behavior was observed. ZMW/LB showed superior adsorption performance under ideal conditions due to enhanced surface heterogeneity and synergistic interactions between Zn and Mn active sites. However, this heterogeneity also results in increased sensitivity to ionic competition and slightly reduced regeneration efficiency. In contrast, ZW/LB exhibited the most stable performance in SWW and the highest reversibility, suggesting more uniform and accessible active sites. MW/LB, although less efficient, demonstrated stronger dye binding and lower desorption efficiency, indicating a greater contribution of surface complexation mechanisms.

From a practical and environmental perspective, the regeneration process involves the use of NaOH, leading to the generation of secondary alkaline effluent containing desorbed dye and dissolved ions.[77] While regeneration reduces solid adsorbent consumption and enhances sustainability, appropriate treatment of this effluent is necessary to prevent secondary environmental contamination.[76] Furthermore, it should be noted that the present study is limited to five regeneration cycles, and extended cycling is required to fully evaluate long-term stability and performance.

Overall, these findings demonstrate that ZW/LB offers the most favorable balance between adsorption efficiency, stability, and resistance to ionic interference under realistic conditions, while ZMW/LB provides higher adsorption capacity under controlled environments. These results are consistent with the mass balance and life cycle assessment analyses, highlighting the importance of optimizing both adsorption performance and operational stability for practical wastewater treatment applications.

3.12 Multivariate interpretation: PCA analysis, correlation matrix, and hierarchical cluster analysis

Multivariate statistical analysis was conducted to elucidate the correlation between the physicochemical characteristics and

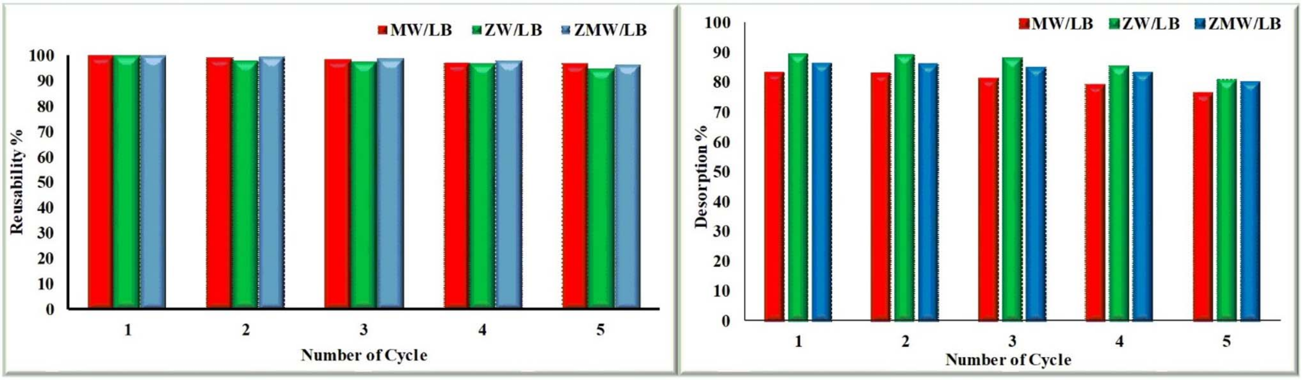

Fig. 17 Reusability and desorption of adsorbents (MW/LB, ZW/LB, and ZMW/LB) for removing AB from SWW.

the performance of adsorption of the MW/LB, ZW/LB, and ZMW/LB composites. According to Principal Component Analysis (PCA),[78] the system can be reliably interpreted in a two-dimensional multivariate space, as illustrated in Table 11, the first principal component PC1 explaining 76.24% of the total variance and the second principal component PC2 corresponding to 23.76%, both PC1 and PC2 fully represent the dataset. PC1 was primarily associated with dye removal efficiency in both pure aqueous and simulated wastewater solutions, as well as textural characteristics such as BET surface area, total pore volume, and average pore diameter.[32,79] The dominance of structural parameters observed in PC1 is consistent with previous studies reporting that the adsorption efficiency of biochar-based adsorbents is strongly governed by surface area, pore structure, and functional groups that facilitate electrostatic attraction and π–π interactions with dye molecules.[80,81]

In contrast, reusability showed a strong negative loading, suggesting an inverse relationship between adsorption efficiency and material stability. These results reveal the presence of a typical efficiency recyclability trade-off commonly observed in porous adsorbent systems. PC2 was mainly influenced by pHpzc, highlighting the significance of surface charge and electrostatic interactions in controlling adsorption behavior, particularly in the presence of competing ions in simulated wastewater. The investigated materials were clearly distinguished by the PCA score plot (Fig. 18A), ZW/LB was positioned in the positive PC1 region, confirming its notable adsorption ability, which is due to its well-developed pore structure and high surface area. Conversely, MW/LB appeared in the negative PC1 region, reflecting lower removal efficiency but higher reusability. ZMW/LB occupied an intermediate position with relatively higher PC2 values, indicating that its adsorption behavior is more strongly affected by surface chemistry and electrostatic interactions.

The correlation matrix analysis[81] further verified the results obtained, as shown in Fig. 18B, which revealed extremely strong positive correlations between structural parameters and removal efficiency, while reusability showed strong negative correlations with most adsorption-related variables. These relationships confirm that surface accessibility and pore structure are strongly dependent on adsorption capacity.

Hierarchical cluster analysis (HCA) was performed[82] to evaluate the similarity relationships among the materials. The dendogram (Fig. 18C) showed that ZW/LB and ZMW/LB cluster together, indicating a high degree of similarity in their structural characteristics and adsorption performance. In contrast, MW/LB formed a separate cluster at a higher linkage distance, confirming its distinct physicochemical properties and adsorption ability. The clustering pattern is completely consistent with the PCA results. From a mechanistic perspective, multivariate analysis indicates that dye removal is primarily governed by pore-filling and surface adsorption processes related to textural characteristics (PC1). On the other hand, the adsorption mechanism enhances electrostatic interactions related to surface charge characteristics (PC2).

As a result, the adsorption process is probably involved in a combination of electrostatic attraction or repulsion based on the pH, physical adsorption inside the porous structure, and potential π–π interactions between dye molecules and the carbon-based framework. These findings support the consistent with adsorption behavior described by pseudo-second-order kinetics and Langmuir–Freundlich isotherm models, suggesting the coexistence of monolayer adsorption and heterogeneous surface interactions. The robustness of the PCA model was verified using Hotelling's T^2 statistics and Q residual analysis.[83] All samples exhibited T^2 values of approximately 1.33, which are significantly below the critical limit at the 95% confidence level, confirming the absence of outliers, as illustrated in Fig. 18D. In addition, Q residual values were negligible due to the complete variance explanation by the first two principal components, indicating an excellent model fit. The Hotelling's T^2 *versus* Q residual plot further confirmed that all observations lie within the acceptable model boundaries, demonstrating that the multivariate model is statistically reliable and stable.

Overall, the combined PCA, correlation matrix, and hierarchical clustering analyses consistently demonstrate that textural properties represent the dominant factors governing adsorption efficiency, while surface chemistry plays a secondary but important role in regulating adsorption behavior and recyclability of the investigated composites.

Table 11 PCA score and loading value for MW/LB, ZW/LB, and ZMW/LB

PCA score	PC1	PC2
MW/LB	−2.54	−0.46
ZW/LB	1.98	−1.00
ZMW/LB	0.56	1.46
Loading	PC1	PC2
BET surface area	0.3790	0.3743
Total pore volume	0.4116	−0.2398
Average pore diameter	0.4131	−0.2314
Removal water	0.3679	0.4085
Removal simulated	0.4191	−0.1934
Reusability	−0.3822	−0.3640
pH_{pzc}	−0.2429	0.6418
Eigenvalue	5.34	1.66
Cumulative percentage	76.24	23.76
Cumulation	76.24	100

3.13 Comparison with previously reported adsorbents

The adsorption performance of the synthesized composites was compared with previously reported tungstate-based and biochar-based adsorbents, as summarized in Table 12. Literature reports indicate that tungstate materials such as $ZnWO_4$, $ZnWO_4$@BCN/N,[25] and $MnWO_4$ (ref. 30) typically exhibit

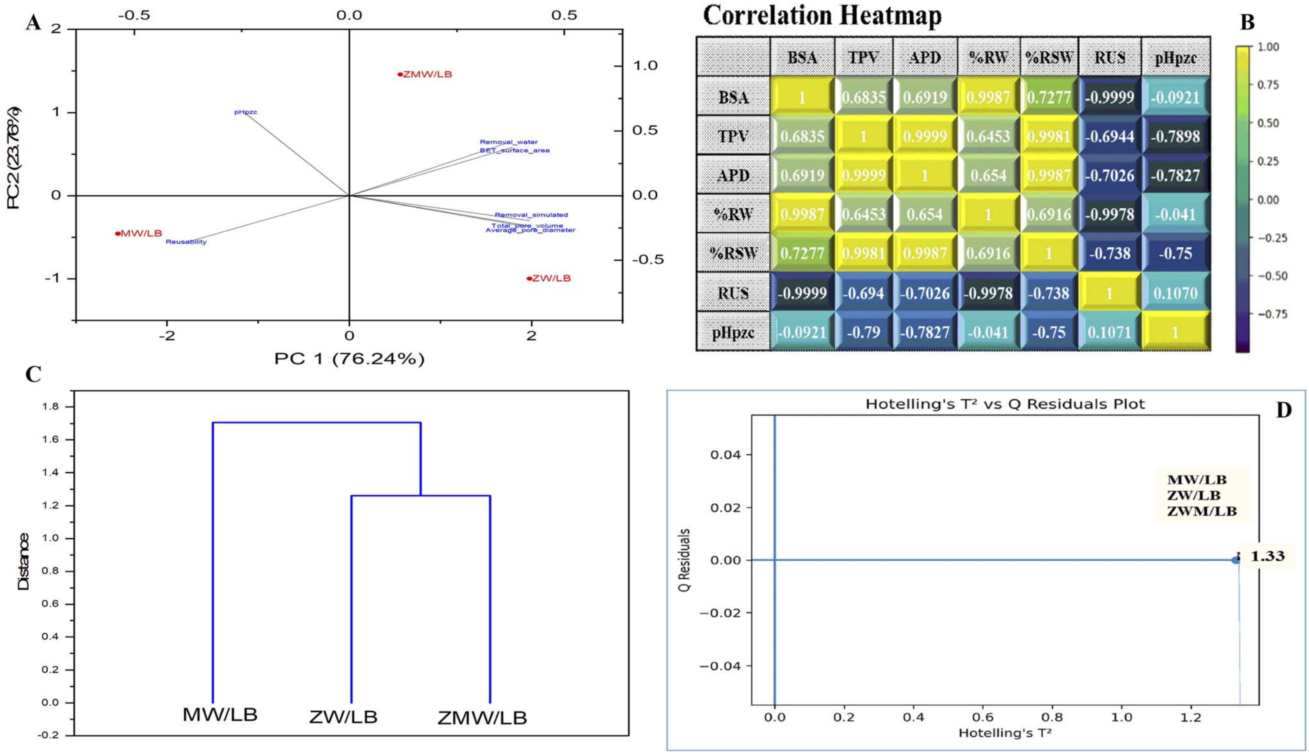

	BSA	TPV	APD	%RW	%RSW	RUS	pHpzc
BSA	1	0.6835	0.6919	0.9987	0.7277	-0.9999	-0.0921
TPV	0.6835	1	0.9999	0.6453	0.9981	-0.6944	-0.7898
APD	0.6919	0.9999	1	0.654	0.9987	-0.7026	-0.7827
%RW	0.9987	0.6453	0.654	1	0.6916	-0.9978	-0.041
%RSW	0.7277	0.9981	0.9987	0.6916	1	-0.738	-0.75
RUS	-0.9999	-0.694	-0.7026	-0.9978	-0.738	1	0.1070
pHpzc	-0.0921	-0.79	-0.7827	-0.041	-0.75	0.1071	1

Fig. 18 (A) PCA Loading score PC1 and PC2, (B) correlation heatmap, (C) hierarchical cluster analysis (HCA), and (D) Hotelling's T^2 *vs.* Q residuals plot for PCA model validation.

adsorption capacities in the range of (218–251 mg g^{-1}) for cationic dyes.

In contrast, conventional adsorbents such as magnesium silicate nanoparticles,[6] magnetic biochar,[84] activated carbon,[85] and modified biochar[86] generally show lower adsorption capacities (27.10–86.95 mg g^{-1}) for dyes such as aniline, aniline blue, and methylene blue.

In comparison, the composites developed in this study exhibited significantly enhanced adsorption performance toward anionic aniline blue, with maximum adsorption capacities of 276.90 mg g^{-1} for MW/LB, 597.99 mg g^{-1} for ZW/LB, and 586.97 mg g^{-1} for ZMW/LB. The superior performance of ZW/LB and ZMW/LB can be attributed to the synergistic combination of metal tungstate nanoparticles and the porous biochar matrix, which enhances surface reactivity, increases the number of accessible adsorption sites, and improves mass transfer through the porous structure.

Furthermore, adsorption occurs under mild conditions (pH ≈ 5, 298 K) and reaches equilibrium within 120 min, supporting the practical applicability of the developed materials. Although the Langmuir model provided a good fit to the equilibrium data, indicating predominant monolayer adsorption, the overall adsorption behavior is governed by a combination of surface interactions and diffusion processes rather than a single mechanism.

Table 12 Comparison of the maximum adsorption capacities of different adsorbents for dye removal reported in the literature

Adsorbent	Dye	Q_{max} (mg g^{-1})	pH	Contact time (min)	T(K)	Surface area (m^2 g^{-1})	Reference
Magnesium silicate nanoparticles	Aniline blue	27.32	4	30	298	90.75	6
Magnetic biochar	Aniline	38.67	3	300	318	118	84
Activated carbon	Aniline	27.10	7	120	308	1070	85
Modified biochar	Methylene blue	86.95	7	30	300	323.04	86
$ZnWO_4$	Malachite green	218.64	8	50	323	24.74	25
$ZnWO_4$@BCN/N	Malachite green	251.75	8	50	323	45.44	
$MnWO_4$	Methylene blue	250	3	10	298	42	30
	Rhodamine B	230	3	2	298	42	
MW/LB	**Aniline blue**	**276.90**	**5**	**120**	**298**	**9.83**	**This study**
ZW/LB	**Aniline blue**	**597.99**	**5**	**120**	**298**	**26.942**	**This study**
ZMW/LB	**Aniline blue**	**586.97**	**5**	**120**	**298**	**31.2**	**This study**

Overall, the results demonstrate that the synthesized composites, particularly ZW/LB and ZMW/LB, outperform many previously reported adsorbents, highlighting their strong potential as efficient and sustainable materials for wastewater treatment.

4 Greenness of the adsorption method and life cycle assessment

To evaluate the environmental sustainability of the proposed adsorption system, a combination of green analytical chemistry metrics (Eco-Scale, AGREE, and GAPI) and a simplified life cycle perspective was applied. While Eco-Scale, AGREE, and GAPI provide valuable insight into the greenness of the analytical and experimental procedures, they do not fully capture the overall environmental impact of material synthesis and application. Therefore, additional discussion on energy consumption, chemical usage, and lifecycle considerations is included to provide a more comprehensive sustainability assessment.

4.1 Eco-scale assessment

The Eco-scale approach, which determine a numerical score based on ideal green conditions (100) minus penalty points for non-green aspects, was used to further quantify the greenness of the method.[33] The penalties for the current study were assigned for: the use of moderately hazardous dye (5 points), inorganic salts (4 points), energy consumption (2 points), waste generation (4 points), instrumental usage (1 point), and energy-intensive adsorbent preparation (8 points). As illustrated in Table 13, the total penalty points amounted to 24, resulting in an Eco-scale score of 76, this score classifies the method as excellent green. However, it is important to note that the major contribution to the penalty score arises from the synthesis stage, particularly the hydrothermal treatment at 160–170 °C, which requires significant energy input.

4.2 AGREE assessment

The AGREE metric was used, which is based on the 12 principles of green analytical chemistry method to evaluate the method.[34] As shown in Fig. 19, the calculated AGREE score was 0.74, indicating good environmental performance. The method exhibits several environmentally favorable aspects, including the use of water as a solvent, elimination of complex sample preparation steps, and minimal chemical consumption. However, certain limitations affecting the score include: use of synthetic dye and inorganic salts, energy consumption during adsorbent synthesis, and generation of regeneration effluent. Despite these factors, the high reusability of the adsorbents (>90% removal efficiency after multiple cycles) significantly improves the overall sustainability by reducing material consumption.

4.3 GAPI assessment

The environmental impact across all procedural steps is graphically displayed utilizing GAPI. A traffic-light color scheme (red = high impact, yellow = moderate impact, green = low impact) was used to evaluate each of the 15 aspects, including sample type, sample size, reagent type, solvent type, energy consumption, waste production, and occupational hazard.[35] The GAPI evaluation provides a qualitative visualization of environmental impact across the entire procedure. Most stages were classified as green, particularly solvent use, sample preparation, and waste volume. Moderate environmental impact (yellow zones) was associated with: reagent toxicity (aniline blue), energy requirements during synthesis, and waste treatment after adsorption/desorption, as shown in Fig. 19. Overall, GAPI confirms that the method has a low-to-moderate environmental footprint, with the synthesis step representing the main environmental burden.

The combined evaluation using AGREE, Eco-Scale, and GAPI demonstrates that the proposed adsorption-based method is efficient, environmentally sustainable, and appropriate for

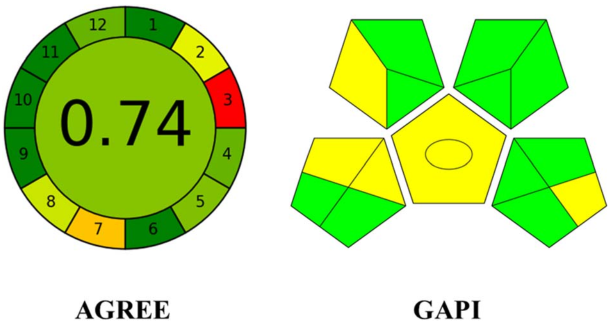

Fig. 19 AGREE and GAPI diagrams illustrating the greenness profile of the adsorption method.

Table 13 Echo scale for the proposed method

Category		Penalty
(1) Chemical used	Aniline blue	5
	Salts (NaCl, $CaCl_2$, $MgSO_4$)	4
(2) Energy consumption	Stirring/shaking	2
(3) Waste generation	Aqueous waste (no organic solvents)	3
(4) Instrumentation	Simple batch setup	1
(5) Adsorbent synthesis	Biochar + metals (Zn, Mn) heating/calcination	8
Excellent green >75	Total penalty	24
	Echo scale	76

Table 14 Environmental impact per functional unit and life cycle assessment

Adsorbent	$Q_{\max}$ (mg g^{-1})	$Q_{\max}$ (g g^{-1})	CO_2 (kg per kg adsorbent)	CO_2 per g dye removed (kg kg^{-1})
MW/LB	291.43	0.291	4.0025	13.75
ZW/LB	426.42	0.426	4.0027	9.39
ZMW/LB	318.86	0.319	4.0025	12.55

green wastewater treatment applications. The use of water as a solvent, minimal chemical consumption, energy-efficient operation, and high adsorbent reusability collectively enhance the environmental performance of the method. The overall assessment confirms that the methodology is in good alignment with the principles of green chemistry, while certain steps, such as material synthesis and the use of moderately hazardous dyes, slightly reduce greenness.

4.4 Life cycle assessment (LCA)

To provide a more comprehensive evaluation of environmental sustainability beyond green analytical metrics, a simplified life cycle assessment (LCA)[87] was conducted by considering both energy consumption and chemical inputs during adsorbent synthesis. This approach allows for a more realistic assessment of environmental impact compared to Eco-Scale, AGREE, and GAPI, which primarily focus on procedural greenness. The total energy consumption for the synthesis of the adsorbents was estimated at approximately 8 kWh, including pyrolysis (4 kWh), hydrothermal treatment (3 kWh), and drying (1 kWh), as shown in Table S4.

In addition, the consumption of precursor chemicals such as $MnCl_2$, $Zn(NO_3)_2$, Na_2WO_4, and NaOH was taken into account using standard CO_2 emission factors[88] (Table S5). Based on these inputs, the total carbon footprint for all synthesized composites was calculated to be approximately 4.00 kg CO_2 per kg adsorbent, with negligible variation among MW/LB, ZW/LB, and ZMW/LB. Although the total CO_2 emissions per unit mass of adsorbent are nearly identical (Table S6), significant differences emerge when the environmental impact is normalized to adsorption performance.

By relating CO_2 emissions to the maximum adsorption capacity ($Q_{\max}$), the environmental efficiency of each material was evaluated in terms of kg CO_2 per kg dye removed. The calculated values were 13.75 kg CO_2 per kg dye for MW/LB, 9.39 kg CO_2 per kg dye for ZW/LB, and 12.55 kg CO_2 per kg dye for ZMW/LB, as shown in Table 14. These results demonstrate that adsorption capacity is the primary factor controlling environmental performance, rather than synthesis-related emissions. The superior environmental efficiency of ZW/LB is attributed to its higher adsorption capacity, which reduces the required adsorbent dosage and overall material consumption. In contrast, MW/LB exhibits the highest environmental impact per functional unit due to its lower adsorption efficiency, despite having a similar synthesis footprint. The bimetallic ZMW/LB composite shows intermediate behavior, reflecting a balance between enhanced adsorption performance and increased compositional complexity. It should be noted that the present LCA represents a simplified estimation and does not include all lifecycle stages, such as large-scale production, transportation, or end-of-life treatment. Furthermore, the regeneration process involving NaOH may contribute to secondary environmental impacts through the generation of alkaline wastewater containing desorbed dye and dissolved ions.[87,89]

Overall, the results indicate that ZW/LB offers the most favorable environmental performance when adsorption efficiency and lifecycle considerations are jointly evaluated. These findings highlight that improving adsorption capacity and optimizing material utilization are key strategies for minimizing the environmental footprint of adsorption-based wastewater treatment systems.

5 Conclusion

Three biochar-based nanocomposites, MW/LB, ZW/LB, and the bimetallic ZMW/LB ($Zn_{0.1}Mn_{0.9}WO_4$/biochar), were successfully synthesized *via* a simple and cost-effective route and evaluated for the removal of aniline blue from aqueous systems. The incorporation of $MnWO_4$ and $ZnWO_4$ into the biochar matrix significantly enhanced adsorption performance through improved surface functionality, increased porosity, and greater accessibility of active sites. The adsorption behavior was strongly influenced by water chemistry. Under ideal conditions (deionized water), ZMW/LB exhibited the highest removal efficiency due to synergistic effects between Zn and Mn species. However, under simulated wastewater conditions, ZW/LB demonstrated superior performance, indicating greater resistance to ionic interference. MW/LB showed lower adsorption efficiency but more stable behavior, suggesting stronger yet fewer active binding sites. All composites exhibited good reusability, retaining more than 95% of their initial removal efficiency after five cycles, with desorption efficiencies ranging from 75% to 90%.

The results indicate that adsorption is predominantly governed by reversible interactions, enabling effective regeneration. From a practical perspective, mass balance analysis confirmed that Zn-containing composites require lower adsorbent dosages, while preliminary cost estimation supports their economic feasibility. Environmental assessment further revealed that, although synthesis-related impacts are similar, significant differences arise when normalized to adsorption performance. In this context, ZW/LB exhibited the lowest environmental footprint per unit of dye removed, highlighting the critical role of adsorption efficiency in determining overall sustainability. Overall, ZW/LB emerges as the most promising material for practical wastewater treatment, offering an optimal balance between adsorption efficiency, stability, and environmental performance. This study underscores the importance of integrating material design, operational conditions, and life-cycle considerations in the development of sustainable adsorption systems.

Author contributions

Kizhan S. Rostam: visualization, validation, methodology, formal analysis, data curation; Khanda F. M. Amin: writing – review & editing, visualization, project administration, methodology, conceptualization.

Conflicts of interest

The authors declare that they have no known competing financial interests or personal relationships that could have appeared to influence the work reported in this paper.

Data availability

The data that support the findings of this study are available on request from the corresponding author. The data are not publicly available due to privacy or ethical restrictions.

Supplementary information (SI): tables and figures. See DOI: https://doi.org/10.1039/d6ra02562e.

Detailed data are included in the result and discussion section; other samples and information are available.

Acknowledgements

During the preparation of this work, the authors used ChatGPT to improve and check the language. After using this tool, the authors reviewed and edited the content as needed and took full responsibility for the publication's content.

References

1 D. Barik, K. M. Rakhi Mol, G. Anand, P. S. Nandamol, D. Das and M. Porel, Environmental Pollutants Such as Endocrine Disruptors/Pesticides/Reactive Dyes and Inorganic Toxic Compounds Metals, Radionuclides, and Metalloids and Their Impact on the Ecosystem, in *Biotechnology for Environmental Sustainability*, ed. P. Verma, Springer Nature, Singapore, 2025, pp. 391–442, DOI: 10.1007/978-981-97-7221-6_15.

2 D. J. Patil and H. S. Grewal, Smart fabrication of $CaFe_2O_4$ using water in-solution organic fuels via facial combustion route and its multidimensional application in dye elimination, *J. Mol. Liq.*, 2024, **411**, 125749, DOI: 10.1016/j.molliq.2024.125749.

3 N. Somaprakash, P. K. Badiya and V. Srinivasan, Green Synthesis of Fluorescent Carbon Dots as a Sustainable Catalyst for Thymol Blue Dye Degradation, *ChemPhysChem*, 2025, **26**, e202500526, DOI: 10.1002/cphc.202500526.

4 T. A. Aragaw, Recovery of iron hydroxides from electro-coagulated sludge for adsorption removals of dye wastewater: Adsorption capacity and adsorbent characteristics, *Surf. Interfaces*, 2020, **18**, 100439, DOI: 10.1016/j.surfin.2020.100439.

5 M. A. Usman, R. A. Aftab, S. Zaidi, S. M. Adnan and R. A. K. Rao, Adsorption of aniline blue dye on activated pomegranate peel: equilibrium, kinetics, thermodynamics and support vector regression modelling, *Int. J. Sci. Environ. Technol.*, 2022, **19**, 8351–8368, DOI: 10.1007/s13762-021-03571-0.

6 A. Magdy, M. E. A. Zaki, M. R. Mostafa, G. G. Mohamed, S. A. Al-Hussain and O. A. Fouad, Integrated kinetic, thermodynamic, and statistical investigation of aniline blue dye removal using magnesium silicate nanoparticles, *Sci. Rep.*, 2025, **15**, 32691, DOI: 10.1038/s41598-025-18726-z.

7 S. El Bourachdi, A. El Amri, A. R. Ayub, Y. Rakcho, F. Moussaoui, M. Lechheb, A. El-Bchiri, O. M. G. Díaz, J. A. Herrera-Melián and A. Lahkimi, Green synthesis of high surface area of reduced graphene oxide via Aloe vera extract: Characterization, DFT mechanistic insights, and enhanced Rhodamine B adsorption using Chitosan@EDTA@rGO composite, *Surf. Interfaces*, 2025, **73**, 107524, DOI: 10.1016/j.surfin.2025.107524.

8 P. Khare, R. K. Patel, S. Sharan and R. Shankar, 8-Recent trends in advanced oxidation process for treatment of recalcitrant industrial effluents, *Advanced Oxidation Processes for Effluent Treatment Plants*, Elsevier, 2021, pp. 137–160, DOI: 10.1016/B978-0-12-821011-6.00008-6.

9 E. S. Mansor, H. Ali and A. Abdel-Karim, Efficient and reusable polyethylene oxide/polyaniline composite membrane for dye adsorption and filtration, *Colloid Interface Sci. Commun.*, 2020, **39**, 100314, DOI: 10.1016/j.colcom.2020.100314.

10 F. F. Taktak and S. Gokce, Eriobotrya japonica-derived TiO_2-carbon dot/Fe_3O_4–chitosan hybrid nanocomposite for adsorptive and photocatalytic removal of crystal violet, *Int. J. Biol. Macromol.*, 2026, **345**, 150323, DOI: 10.1016/j.ijbiomac.2026.150323.

11 S.-R. Jin, K.-Y. Lee, S.-H. Park, J.-M. Cheon, S. B. Kang and C.-W. Cho, Amine-functionalized cellulose for the efficient removal of anionic micropollutants from aqueous environments: Development, characterization, and modeling, *J. Water Process Eng.*, 2025, **75**, 107940, DOI: 10.1016/j.jwpe.2025.107940.

12 M. Umar, A. Doho, A. Abubakar, H. A. Kadir and S. S. K. Hausa, Remediation of Groundwater Containing Gentian Violet Dye Using Hydrogel, *Surf. Colloid Sci.*, 2025, **7**, 31–39, DOI: 10.11648/j.css.20250702.11.

13 N. F. A. Neto, P. M. Oliveira, R. M. Nascimento, C. A. Paskocimas, M. R. D. Bomio and F. V. Motta, Influence of pH on the morphology and photocatalytic activity of CuO obtained by the sonochemical method using different surfactants, *Ceram. Int.*, 2019, **45**, 651–658, DOI: 10.1016/j.ceramint.2018.09.224.

14 A. M. Aljeboree, U. A.-R. Hussein, A. F. Alkaim, S. Abd, F. H. Alsultany and U. S. Altimari, Phosphoric acid-

activated carbon derived from Ziziphus seed waste for crystal Violet removal: insights from experiments and molecular dynamics simulations, *J. Iran. Chem. Soc.*, 2025, **23**, 12, DOI: 10.1007/s13738-025-03300-1.

15 S. Gürsoy, N. K. Zeytinci, B. T. Zaman, S. Bakırdere and E. Öztürk Er, Study of linear and nonlinear isotherm and kinetic parameters of hexavalent chromium adsorption onto reduced graphene oxide coated iron oxide, *Sci. Rep.*, 2025, **15**, 25206, DOI: 10.1038/s41598-025-97588-x.

16 B. K. Majeed, K. A. Rashid and D. M. S. Shwan, An eco-friendly approach to soil remediation: evaluating clay–biochar composite for used motor oil removal through kinetic, isotherm, and thermodynamic models, *Environ. Sci. Process. Impacts*, 2025, **27**, 2982–3001, DOI: 10.1039/D5EM00404G.

17 K. D. Otaif and E. A. Mergani, Sustainable Dipterygium glaucum-based hydrochars for the efficient removal of organic dyes from wastewater, *J. Mol. Liq.*, 2025, **436**, 128278, DOI: 10.1016/j.molliq.2025.128278.

18 S. E. A. Hameed, W. M. A. El-Maaty, E. A. Gomaa and F. S. Awad, PAR-intercalated Mg/Al layered double hydroxide for efficient adsorption of acid fuchsin: experimental study and molecular docking insights, *RSC Adv.*, 2026, **16**, 6408–6420, DOI: 10.1039/D5RA08890A.

19 H. Guan, Y. Fan, W. Wang, Q. Wang, Y. Chen and S. Ruan, Xylene detection performances of core-shelled $MnWO_4$@C composites synthesized by functionalizing carbon microsphere template, *Sens. Actuators, B*, 2024, **407**, 135478, DOI: 10.1016/j.snb.2024.135478.

20 M. Mączka, M. Ptak, A. Pikul, L. Kępiński, P. E. Tomaszewski and J. Hanuza, Phonon and magnetic properties of nanocrystalline $MnWO_4$ prepared by hydrothermal method, *Vib. Spectrosc.*, 2012, **58**, 163–168, DOI: 10.1016/j.vibspec.2011.12.010.

21 V. Faka, S. Tsoumachidou, M. Moschogiannaki, G. Kiriakidis, I. Poulios and V. Binas, $ZnWO_4$ nanoparticles as efficient photocatalyst for degradation of para-aminobenzoic acid: Impact of annealing temperature on photocatalytic performance, *J. Photochem. Photobiol. Chem.*, 2021, **406**, 113002, DOI: 10.1016/j.jphotochem.2020.113002.

22 A. Somdee and S. Wannapop, Enhanced photocatalytic behavior of ZnO nanorods decorated with a Au, $ZnWO_4$, and Au/$ZnWO_4$ composite: Synthesis and characterization, *Colloid Interface Sci. Commun.*, 2022, **47**, 100591, DOI: 10.1016/j.colcom.2022.100591.

23 R. Sreeja, T. Shahanas and G. Harichandran, g-C_3N_4 Modified $MnWO_4$ nanorods as high-performance electrode materials for asymmetric supercapacitors, *Electrochim. Acta*, 2025, **521**, 145895, DOI: 10.1016/j.electacta.2025.145895.

24 D. R. Kandel, P. Gaudel, M. B. Poudel, W. Yun and J. Lee, Single- and multi-metal engineered, functionalized hybrid biochars for heavy metal adsorption: synthesis, structure-function relationships, and coordination mechanisms, *Coord. Chem. Rev.*, 2026, **555**, 217521, DOI: 10.1016/j.ccr.2025.217521.

25 H. L. Abubakar, J. O. Tijani, A. S. Abdulkareem, T. C. Egbosiuba, M. Abdullahi, S. Mustapha and E. A. Ajiboye, Effective removal of malachite green from local dyeing wastewater using zinc-tungstate-based materials, *Heliyon*, 2023, **9**, e19167, DOI: 10.1016/j.heliyon.2023.e19167.

26 M. Govindhan and K. Sukumar, Strategic design and preparation of $Zn_{1-x}Mn_xWO_4$ materials for high-performance hybrid supercapacitor application, *J. Power Sources*, 2025, **658**, 238287, DOI: 10.1016/j.jpowsour.2025.238287.

27 N. Hagemann, K. Spokas, H.-P. Schmidt, R. Kägi, M. A. Böhler and T. D. Bucheli, Activated Carbon, Biochar and Charcoal: Linkages and Synergies across Pyrogenic Carbon's ABCs, *Water*, 2018, **10**, 182, DOI: 10.3390/w10020182.

28 S. Satyam and S. Patra, Innovations and challenges in adsorption-based wastewater remediation: A comprehensive review, *Heliyon*, 2024, **10**, e29573, DOI: 10.1016/j.heliyon.2024.e29573.

29 M. S. Hassan, T. Amna, S. S. Al-Deyab, H.-C. Kim and M.-S. Khil, Monodispersed 3D $MnWO_4$-TiO_2 composite nanoflowers photocatalysts for environmental remediation, *Curr. Appl. Phys.*, 2015, **15**, 753–758, DOI: 10.1016/j.cap.2015.03.022.

30 D. P. Dutta, A. Mathur, J. Ramkumar and A. K. Tyagi, Sorption of dyes and Cu(II) ions from wastewater by sonochemically synthesized $MnWO_4$ and $MnMoO_4$, *RSC Adv.*, 2014, **4**, 37027, DOI: 10.1039/C4RA07618D.

31 R. M. Kakhki, F. YereyehZadeh and M. Mohammadpoor, Machine Learning Optimized Photocatalytic Degradation of Tetracycline Using Sulfur-Doped Zinc oxide/Chitosan Nanocomposites, *J. Polym. Environ.*, 2025, **33**, 5042–5065, DOI: 10.1007/s10924-025-03700-7.

32 O. Mouhtady, E. Obeid, M. Abu-samha, K. Younes and N. Murshid, Evaluation of the Adsorption Efficiency of Graphene Oxide Hydrogels in Wastewater Dye Removal: Application of Principal Component Analysis, *Gels*, 2022, **8**, 447, DOI: 10.3390/gels8070447.

33 A. Gałuszka, Z. M. Migaszewski, P. Konieczka and J. Namieśnik, Analytical Eco-Scale for assessing the greenness of analytical procedures, *TrAC, Trends Anal. Chem.*, 2012, **37**, 61–72, DOI: 10.1016/j.trac.2012.03.013.

34 F. Pena-Pereira, W. Wojnowski and M. Tobiszewski, AGREE-Analytical GREEnness Metric Approach and Software, *Anal. Chem.*, 2020, **92**, 10076–10082, DOI: 10.1021/acs.analchem.0c01887.

35 J. Płotka-Wasylka, A new tool for the evaluation of the analytical procedure: Green Analytical Procedure Index, *Talanta*, 2018, **181**, 204–209, DOI: 10.1016/j.talanta.2018.01.013.

36 S. Soudagar, S. Akash, M. Sree Venkat, V. Rao Poiba and M. Vangalapati, Adsorption of methylene blue dye on nano graphene oxide-thermodynamics and kinetic studies, *Mater. Today Proc.*, 2022, **59**, 667–672, DOI: 10.1016/j.matpr.2021.12.199.

37 A. A. kaka Mohammed, K. J. J. Al-Salihi and R. F. HamaRawf, Synthesis, characterization, and application of low-cost Mg-Al/CO_3 and Ni-Al/CO_3 layered double hydroxides (LDHs) as adsorbents for the removal of aniline blue dye from aqueous solutions: adsorption isotherms, kinetics, and thermodynamic studies, *RSC Adv.*, 2025, **15**, 27630, DOI: 10.1039/D5RA04856G.
38 H. Ouachtak, A. El Guerdaoui, R. El Haouti, R. Haounati, H. Ighnih, Y. Toubi, F. Alakhras, R. Rehman, N. Hafid, A. A. Addi and M. L. Taha, Combined molecular dynamics simulations and experimental studies of the removal of cationic dyes on the eco-friendly adsorbent of activated carbon decorated montmorillonite Mt@AC, *RSC Adv.*, 2023, **13**, 5027, DOI: 10.1039/D2RA08059A.
39 D. Rallet, A. Paltahe, C. Tsamo and B. Loura, Synthesis of clay-biochar composite for glyphosate removal from aqueous solution, *Heliyon*, 2022, **8**, e09112, DOI: 10.1016/j.heliyon.2022.e09112.
40 J. O. Tijani, M. N. Abdullahi, M. T. Bankole, S. Mustapha, T. C. Egbosiuba, M. M. Ndamitso, A. S. Abdulkareem and E. Muzenda, Photocatalytic and toxicity evaluation of local dyeing wastewater by aluminium/boron doped WO3 nanoparticles, *J. Water Process Eng.*, 2021, **44**, 102376, DOI: 10.1016/j.jwpe.2021.102376.
41 S. Karthikadevi, S. Mullainathan, N. Jabena Begum, S. Manimaran, N. Muruganantham, R. Govindharaju and K. Ravichandran, Multiple synergistic benefits of the composite partners $ZnWO_4$ and activated carbon: Augmented photocatalytic performance, *Inorg. Chem. Commun.*, 2025, **181**, 115204, DOI: 10.1016/j.inoche.2025.115204.
42 S. L. Prabavathi, K. Saravanakumar, G. Mamba and V. Muthuraj, 1D/2D $MnWO_4$ nanorods anchored on g-C3N4 nanosheets for enhanced photocatalytic degradation ofloxacin under visible light irradiation, *Colloids Surf., A*, 2019, **581**, 123845, DOI: 10.1016/j.colsurfa.2019.123845.
43 Y. Verma, M. Naushad, A. García-Peñas, A. Kumar, P. Dhiman and G. Sharma, Exploring the potential of MnWO4/MXene/carbon xerogel photocatalyst for photo efficient degradation of crystal violet, *Chem. Eng. Res. Des.*, 2025, **219**, 235–248, DOI: 10.1016/j.cherd.2025.05.053.
44 M. A. Khedr, A. I. Ahmed and E. A. El-sharkawy, Enhanced Electrochemical Performance of Er_2O_3/$ZnWO_4$ Composite for High-Efficiency Supercapacitor Applications, *Mansoura J. Chem.*, 2025, **68**, 37–42, DOI: 10.21608/mjcc.2025.388919.1013.
45 T. Ma, Z. Li, G. Wang, J. Zhang and Z. Wang, Efficient Visible-Light Driven Photocatalytic Hydrogen Production by Z-Scheme $ZnWO_4$/$Mn_{0.5}Cd_{0.5}S$ Nanocomposite without Precious Metal Cocatalyst, *Catalysts*, 2022, **12**, 1527, DOI: 10.3390/catal12121527.
46 Q. Xiao, S. Li, B. Leng, Z. Yao, Z. Yu, C. Xing, B. Zhang, X. Tong and Y. Hou, Light-driven decontamination of co-existing organic pollutants by $Zn_3In_2S_6$/$ZnWO_4$ heterojunction: Degradation behavior and mechanisms, *J. Environ. Chem. Eng.*, 2026, **14**, 121483, DOI: 10.1016/j.jece.2026.121483.
47 A. E. B. Lima, M. Assis, A. L. S. Resende, H. L. S. Santos, L. H. Mascaro, E. Longo, R. S. Santos, L. S. Cavalcante and G. E. Luz Jr, $CuWO_4|MnWO_4$ heterojunction thin film with improved photoelectrochemical and photocatalytic properties using simulated solar irradiation, *J. Solid State Electrochem.*, 2022, **26**, 997–1011, DOI: 10.1007/s10008-022-05143-9.
48 F. Sedighi, M. Ghiyasiyan-Arani and M. Behpour, Biomass-derived porous carbon-supported $MnWO_4$/$CeVO_4$ nanocomposites: Influence of solvent and natural surfactant on morphology and electrochemical hydrogen storage performance, *Energy Nexus*, 2025, **20**, 100548, DOI: 10.1016/j.nexus.2025.100548.
49 P. C. Nagajyothi, K. Yoo, R. Ramaraghavulu and J. Shim, Hydrothermal Synthesis of $MnWO_4$@GO Composite as Non-Precious Electrocatalyst for Urea Oxidation, *Nanomaterials*, 2021, **12**, 85, DOI: 10.3390/nano12010085.
50 L. Zhang, Z. Wang, L. Wang, Y. Xing, X. Li and Y. Zhang, Electrochemical performance of $ZnWO_4$/CNTs composite as anode materials for lithium-ion battery, *Appl. Surf. Sci.*, 2014, **305**, 179–185, DOI: 10.1016/j.apsusc.2014.03.035.
51 N. Omrani, A. Nezamzadeh-Ejhieh and M. Alizadeh, Brief study on the kinetic aspect of photodegradation of sulfasalazine aqueous solution by cuprous oxide/cadmium sulfide nanoparticles, *Desalination Water Treat.*, 2019, **162**, 290–302, DOI: 10.5004/dwt.2019.24352.
52 S. K. Sharma, K. Sudarshan, D. Sen and P. K. Pujari, Microenvironment of mesopores of MCM-41 supported CuO catalyst: An investigation using positronium probe, *J. Solid State Chem.*, 2019, **274**, 10–17, DOI: 10.1016/j.jssc.2019.03.015.
53 B. Mikuła and B. Puzio, Determination of trace metals by ICP-OES in plant materials after preconcentration of 1,10-phenanthroline complexes on activated carbon, *Talanta*, 2007, **71**, 136–140, DOI: 10.1016/j.talanta.2006.03.041.
54 G. Celoria, V. Miglio, G. Paul, C. Bisio, G. Golemme and E. Boccaleri, Silica Particles Derived from Natural Kaolinite for the Removal of Rhodamine B from Polluted Water, *Processes*, 2022, **10**, 964, DOI: 10.3390/pr10050964.
55 N. F. A. Neto, Y. G. Oliveira, C. A. Paskocimas, M. R. D. Bomio and F. V. Motta, Increase of antimicrobial and photocatalytic properties of silver-doped PbS obtained by sonochemical method, *J. Mater. Sci.: Mater. Electron.*, 2018, **29**, 19052–19062, DOI: 10.1007/s10854-018-0031-z.
56 J. Huang and L. Gao, One-Step Fabrication of $ZnWO_4$ Hollow Spheres by Nanoparticle Aggregation and Ripening in Alcohol Solution, *J. Am. Ceram. Soc.*, 2006, **89**, 3877–3880, DOI: 10.1111/j.1551-2916.2006.01318.x.
57 X. He, R. Büchel, R. Figi, Y. Zhang, Y. Bahk, J. Ma and J. Wang, High-performance carbon/MnO_2 micromotors and their applications for pollutant removal, *Chemosphere*, 2019, **219**, 427–435, DOI: 10.1016/j.chemosphere.2018.12.051.
58 Z. Zhang and J. Kong, Novel magnetic Fe_3O_4@C nanoparticles as adsorbents for removal of organic dyes from aqueous solution, *J. Hazard. Mater.*, 2011, **193**, 325–329, DOI: 10.1016/j.jhazmat.2011.07.033.

59 X. Zhang, D. Zhen, F. Liu, R. Chen, Q. Peng and Z. Wang, An achieved strategy for magnetic biochar for removal of tetracyclines and fluoroquinolones: Adsorption and mechanism studies, *Bioresour. Technol.*, 2023, **369**, 128440, DOI: 10.1016/j.biortech.2022.128440.

60 H. Y. Sharef, A. F. Jalal, B. M. Ibrahim, N. A. Fakhre and I. N. Qader, New ion-imprinted polymer for selective removal of Cu^{2+} ion in aqueous solution using extracted Aloe Vera leaves as a monomer, *Int. J. Biol. Macromol.*, 2023, **239**, 124318, DOI: 10.1016/j.ijbiomac.2023.124318.

61 H. Roy, Md. S. Islam, M. T. Arifin and S. H. Firoz, Chitosan-ZnO decorated Moringa oleifera seed biochar for sequestration of methylene blue: Isotherms, kinetics, and response surface analysis, *Environ. Nanotechnol. Monit. Manag.*, 2022, **18**, 100752, DOI: 10.1016/j.enmm.2022.100752.

62 T. C. Egbosiuba, A. S. Abdulkareem, A. S. Kovo, E. A. Afolabi, J. O. Tijani, M. Auta and W. D. Roos, Ultrasonic enhanced adsorption of methylene blue onto the optimized surface area of activated carbon: Adsorption isotherm, kinetics and thermodynamics, *Chem. Eng. Res. Des.*, 2020, **153**, 315–336, DOI: 10.1016/j.cherd.2019.10.016.

63 N. Sadegh, H. Haddadi, P. Arabkhani, A. Asfaram and F. Sadegh, Simultaneous elimination of Rhodamine B and Malachite Green dyes from the aqueous sample with magnetic reduced graphene oxide nanocomposite: Optimization using experimental design, *J. Mol. Liq.*, 2021, **343**, 117710, DOI: 10.1016/j.molliq.2021.117710.

64 M. A. Djilali, H. Mekatel, M. Mellal and M. Trari, Synthesis and characterization of $MgCo_2O_4$ nanoparticles: Application to removal of Ni^{2+} in aqueous solution by adsorption, *J. Alloys Compd.*, 2022, **907**, 164498, DOI: 10.1016/j.jallcom.2022.164498.

65 M. E. Mahmoud, R. M. El-Sharkawy and G. A. A. Ibrahim, A novel bionanocomposite from doped lipase enzyme into magnetic graphene oxide-immobilized-cellulose for efficient removal of methylene blue and malachite green dyes, *J. Mol. Liq.*, 2022, **368**, 120676, DOI: 10.1016/j.molliq.2022.120676.

66 S. M. Omar and A. F. Jalal, Cost-effective adsorption of pharmaceutical pollutant from aqueous solution using novel activated carbon derived from sumac seed, *Int. J. Environ. Anal. Chem.*, 2026, **106**, 463–487, DOI: 10.1080/03067319.2025.2518309.

67 T. V. Tran, D. T. C. Nguyen, P. S. Kumar, A. T. M. Din, A. S. Qazaq and D.-V. N. Vo, Green synthesis of Mn_3O_4 nanoparticles using Costus woodsonii flowers extract for effective removal of malachite green dye, *Environ. Res.*, 2022, **214**, 113925, DOI: 10.1016/j.envres.2022.113925.

68 M. N. Garcia Gonzalez, R. Quiroga-Flores and P. Börjesson, Life cycle assessment of a nanomaterial-based adsorbent developed on lab scale for cadmium removal: Comparison of the impacts of production, use and recycling, *Clean. Environ. Syst.*, 2022, **4**, 100071, DOI: 10.1016/j.cesys.2022.100071.

69 J. M. Gómez, J. Galán, A. Rodríguez and G. M. Walker, Dye adsorption onto mesoporous materials: pH influence, kinetics and equilibrium in buffered and saline media, *J. Environ. Manag.*, 2014, **146**, 355–361, DOI: 10.1016/j.jenvman.2014.07.041.

70 M. Cetina, P. Mihovilović, A. Pešić and B. Vojnović, Influence of Ionic Strength and Temperature on the Adsorption of Reactive Black 5 Dye by Activated Carbon: Kinetics, Mechanisms and Thermodynamics, *Molecules*, 2025, **30**, 2593, DOI: 10.3390/molecules30122593.

71 H. Molavi, A. Pourghaderi and A. Shojaei, Experimental Study on the Influence of Initial pH, Ionic Strength, and Temperature on the Selective Adsorption of Dyes onto Nanodiamonds, *J. Chem. Eng. Data*, 2019, **64**, 1508–1514, DOI: 10.1021/acs.jced.8b01091.

72 F. A. Razmi, N. Ngadi, S. Wong, I. M. Inuwa and L. A. Opotu, Kinetics, thermodynamics, isotherm and regeneration analysis of chitosan modified pandan adsorbent, *J. Clean. Prod.*, 2019, **231**, 98–109, DOI: 10.1016/j.jclepro.2019.05.228.

73 A. Asfaram, M. Ghaedi, S. Hajati, A. Goudarzi and E. A. Dil, Screening and optimization of highly effective ultrasound-assisted simultaneous adsorption of cationic dyes onto Mn-doped Fe_3O_4-nanoparticle-loaded activated carbon, *Ultrason. Sonochem.*, 2017, **34**, 1–12, DOI: 10.1016/j.ultsonch.2016.05.011.

74 Y. S. Al-Degs, M. I. El-Barghouthi, A. H. El-Sheikh and G. M. Walker, Effect of solution pH, ionic strength, and temperature on adsorption behavior of reactive dyes on activated carbon, *Dyes Pigm.*, 2008, **77**, 16–23, DOI: 10.1016/j.dyepig.2007.03.001.

75 S. Yadav, A. Asthana, A. K. Singh, R. Chakraborty, S. S. Vidya, Md. Abu Bin Hasan Susan and S. A. C. Carabineiro, Adsorption of cationic dyes, drugs and metal from aqueous solutions using a polymer composite of magnetic/β-cyclodextrin/activated charcoal/Na alginate: Isotherm, kinetics and regeneration studies, *J. Hazard. Mater.*, 2021, **409**, 124840, DOI: 10.1016/j.jhazmat.2020.124840.

76 D. T. C. Nguyen, H. H. Dang, D.-V. N. Vo, L. G. Bach, T. D. Nguyen and T. V. Tran, Biogenic synthesis of MgO nanoparticles from different extracts (flower, bark, leaf) of Tecoma stans (L.), and their utilization in selected organic dyes treatment, *J. Hazard. Mater.*, 2021, **404**, 124146, DOI: 10.1016/j.jhazmat.2020.124146.

77 F. Moradnia, S. Taghavi Fardood, A. Ramazani, B. Min, S. W. Joo and R. S. Varma, Magnetic $Mg_{0.5}Zn_{0.5}FeMnO_4$ nanoparticles: Green sol-gel synthesis, characterization, and photocatalytic applications, *J. Clean. Prod.*, 2021, **288**, 125632, DOI: 10.1016/j.jclepro.2020.125632.

78 J. F. Hair, *Multivariate Data Analysis*, Cengage, Andover, Hampshire, 8th edn, 2019.

79 G. Vyavahare, R. Patil, R. Gurav, F. M. Shorobi, S. Kadam, J. Jadhav and J. H. Park, Investigating the efficacy of biochar produced from agro-waste for basic fuchsin dye removal: Kinetics, isotherm, and thermodynamic studies, *J. Indian Chem. Soc.*, 2024, **101**, 101278, DOI: 10.1016/j.jics.2024.101278.

80 J. Xu, M. Fu, Q. Ma, X. Zhang, C. You, Z. Shi, Q. Lin, X. Wang and W. Feng, Modification of biochar by phosphoric acid *via* wet pyrolysis and using it for adsorption of methylene blue,

RSC Adv., 2023, **13**, 15327–15333, DOI: 10.1039/D3RA00680H.

81 K. Younes K, Y. Kharboutly, M. Antar, H. Chaouk, E. Obeid, O. Mouhtady, M. Abu-samha, J. Halwani and N. Murshid, Application of Unsupervised Learning for the Evaluation of Aerogels' Efficiency towards Dye Removal-A Principal Component Analysis (PCA) Approach, *Gels*, 2023, **9**, 327, DOI: 10.3390/gels9040327.

82 J. Lladó, F. López, J. M. Rossell, C. Lao-Luque, R. R. Gil, E. Fuente and B. Ruiz, Multivariate analysis of pharmaceutical pollutants adsorption in aqueous media with tailored waste-based carbonaceous adsorbent materials and commercial activated carbons, *Sustain. Chem. Pharm.*, 2024, **38**, 101453, DOI: 10.1016/j.scp.2024.101453.

83 A. Zaffar, M. R. Prabhakar, S. Jayaraman, C. Liu and P. Balasubramanian, Multivariate Optimization of Electrochemical Struvite Precipitation from Wastewater Using Principal Component Analysis, *ACS ES&T Water*, 2025, **5**, 2361–2372, DOI: 10.1021/acsestwater.4c01254.

84 S. Sutar and J. Jadhav, A comparative assessment of the methylene blue dye adsorption capacity of natural biochar versus chemically altered activated carbons, *Bioresour. Technol. Rep.*, 2024, **25**, 101726, DOI: 10.1016/j.biteb.2023.101726.

85 Y. Gu, Y. Xue and D. Zhang, Adsorption of aniline by magnetic biochar with high magnetic separation efficiency, *Environ. Pollut. Bioavailab.*, 2021, **33**, 66–75, DOI: 10.1080/26395940.2021.1920469.

86 H. Li, L. Liu, J. Cui, J. Cui, F. Wang and F. Zhang, High-efficiency adsorption and regeneration of methylene blue and aniline onto activated carbon from waste edible fungus residue and its possible mechanism, *RSC Adv.*, 2020, **10**, 14262, DOI: 10.1039/D0RA01245A.

87 J. Artz, T. E. Müller, K. Thenert, J. Kleinekorte, R. Meys, A. Sternberg, A. Bardow and W. Leitner, Sustainable Conversion of Carbon Dioxide: An Integrated Review of Catalysis and Life Cycle Assessment, *Chem. Rev.*, 2018, **118**, 434–504, DOI: 10.1021/acs.chemrev.7b00435.

88 R. G. Grim, A. Badgett, W. A. Braunecker, M. T. Guarnieri, S. E. Habas, C. Hahn, K. Neyerlin, A. Prajapati, D. A. Ruddy and R. Z. Walker, The Chemistry of CO2 Conversion: A Review, *Chem. Rev.*, 2026, **126**, 5028–5082, DOI: 10.1021/acs.chemrev.5c00361.

89 J. Saleem, Z. Khalid Baig Moghal, F. Tahir, T. Al-Ansari, A. I. Osman and G. McKay, Life cycle assessment of high-value activated carbon production based on mass and functional performance metrics, *Sci. Rep.*, 2025, **15**, 32797, DOI: 10.1038/s41598-025-16300-1.